

Trans-dimensional surface reconstruction with different classes of parameterization

Rhys Hawkins¹, Thomas Bodin¹, Malcolm Sambridge², Gaël Choblet³, Laurent Husson⁴

¹Laboratoire de Géologie de Lyon Terre, Planètes, Environnement, Ecole Normale Supérieure de Lyon, Lyon, France

²Research School of Earth Sciences, Australian National University, Canberra, Australia

³Université de Nantes, CNRS, Laboratoire de Planétologie et Géodynamique, Nantes, France.

⁴Université Grenoble Alpes, CNRS, ISTerre, Grenoble, France

Key Points:

- We present a new software for trans-dimensional surface reconstruction incorporating Hierarchical Error estimation, Hamiltonian Monte Carlo, and Parallel Tempering.
- We propose two alternative parameterizations to the ubiquitous Voronoi cells: Delaunay triangulation and Clough-Tocher interpolation.
- These alternate parameterizations may open up the application of trans-dimensional surface reconstruction to a wider variety of geophysical problems.

18 **Abstract**

19 The use of Bayesian trans-dimensional sampling in 2D and 3D imaging problems
 20 has recently become widespread in geophysical inversion. Its benefits include its spatial
 21 adaptability to the level of information present in the data and the ability to produce
 22 uncertainty estimates. The most used parameterization in Bayesian trans-dimensional
 23 inversions is Voronoi cells. Here we introduce a general software, TransTessellate2D, that
 24 allows 2D trans-dimensional inference with Voronoi cells and two alternative underly-
 25 ing parameterizations, Delaunay triangulation with linear interpolation and Clough-Tocher
 26 interpolation, which utilize the same algorithm but result in either C^0 or C^1 continu-
 27 ity. We demonstrate that these alternatives are better suited to the recovery of smooth
 28 models, and show that the posterior probability solution is less susceptible to multi-modalities
 29 which can complicate the interpretation of model parameter uncertainties.

30 **1 Introduction**

31 Geophysical inverse problems regularly involve observations with spatially vary-
 32 ing sensitivity to the Earth’s properties of interest. Examples include seismic tomogra-
 33 phy where the location of earthquakes are concentrated at tectonic plate boundaries or
 34 fault zones (Rawlinson, Fichtner, Sambridge, & Young, 2014), or assessing regional coastal
 35 inundation rates where tide gauge observations are sparsely located (Church & White,
 36 2011), or climate reconstructions from bore hole temperature records (Hopcroft, Gallagher,
 37 & Pain, 2009), or estimates of global heat flow (Davies, 2013). A major problem is that
 38 the irregular spatial distribution the observations can cause instabilities in the inverse
 39 problem when regular grids are used. In a general inverse problem we formulate the prob-
 40 lem as

$$\mathbf{G}\mathbf{m} = \mathbf{d} + \epsilon, \tag{1}$$

41 where \mathbf{d} is a vector of our observations, \mathbf{m} the vector of unknown Earth model pa-
 42 rameters, \mathbf{G} the forward model operator and ϵ representing errors. An irregular distri-
 43 bution of observations, where parts of grid are not constrained by the observations can
 44 result in a matrix \mathbf{G} that is not full rank, in which case \mathbf{G} is not invertable. Alterna-
 45 tively, or \mathbf{G} may have one or more rows with near linear dependence resulting in poor
 46 conditioning of the inverse.

47 A standard approach to this problem is to regularize the problem by either damp-
48 ping the solution towards a reference model or by penalizing large spatial gradients through
49 maximization of smoothness measures. Such damping or smoothing regularization are
50 commonly performed uniformly across and while there exist criteria for the selection of
51 these weights, they are not without limitations (Hanke, 1996; Hansen, 1999).

52 This problem has been well recognized within the community and various adap-
53 tive parameterization schemes have been implemented. These methods typically use a
54 heuristic metric, such as the density of data coverage, in order to determine if a region
55 should be inverted at a finer resolution (Chiao & Kuo, 2001; Inoue, Fukao, Tanabe, &
56 Ogata, 1990; Káráson & van der Hilst, 2001; Sambridge & Faletič, 2003).

57 Where observations can be related to a continuous Earth model through sensitiv-
58 ity kernels in linear or near-linear problems, another method is the Backus-Gilbert or
59 Optimal Local Averages (Backus, 1970a, 1970b, 1970c). In this approach the Earth model
60 is continuously parameterized and the problem is one of solving for a local average at
61 a point by using resolution constraints based on the sensitivity kernels. In the original
62 formulation, this required a large computational effort for each point of the domain which
63 limited application of this style of inversion. An alternate formulation was developed in
64 the helio-seismology community which improves the efficiency of Backus-Gilbert inver-
65 sions (Pijpers & Thompson, 1992) and has recently been applied to large scale seismic
66 tomography problems (Zaroli, 2016).

67 Recently more general approaches have been proposed that use priors generated
68 from training data (Lochbühler, Vrugt, Sadegh, & Linde, 2015) or structural informa-
69 tion (de Pasquale & Linde, 2017) as a way to impose spatially varying model correla-
70 tion. Alternatively, prior constraints can be controlled by hyper-parameters in a hier-
71 archical Bayesian framework (Malinverno & Briggs, 2004; Valentine & Sambridge, 2018).
72 Bayesian techniques use probabilistic prior information in conjunction with observations
73 to obtain a posterior probability distribution of model parameters, commonly using Markov
74 chain Monte Carlo (MCMC) methods (Mosegaard & Tarantola, 1995; Sambridge & Mosegaard,
75 2002). In MCMC methods, rather than searching for a single optimal model, an ensem-
76 ble of plausible models are computed from which in addition to optimal models, estimates
77 of uncertainty can be obtained.

78 An extension to traditional fixed model dimension MCMC inversion, where the num-
79 ber of model parameters remains fixed, is trans-dimensional or reversible jump MCMC
80 (rjMCMC) (Denison, Holmes, Mallick, & Smith, 2002; Green, 1995). In this method the
81 dimension of the model, that is the number of unknown parameters, is inverted for as
82 part of the process. The often repeated claim of trans-dimensional inversion is that it
83 results in a parsimonious solution, that is, the resulting Markov chain ensemble will con-
84 verge toward models with an efficient number of parameters required to predict the ob-
85 servations within noise levels (neither under-parameterized nor over-parameterized mod-
86 els). This general approach has been utilized in a number of geophysical inverse prob-
87 lems across various disciplines (Bodin, Salmon, Kennett, & Sambridge, 2012; Bodin &
88 Sambridge, 2009; Burdick & Lekić, 2017; Dettmer, Dosso, & Holland, 2011; Dettmer et
89 al., 2016; Dettmer, Molnar, Steininger, Dosso, & Cassidy, 2012; Galetti, Curtis, Baptie,
90 Jenkins, & Nicolson, 2016; Hawkins, Brodie, & Sambridge, 2017; Malinverno, 2002; Olug-
91 boji, Lekic, & McDonough, 2017; Piana Agostinetti, Giacomuzzi, & Malinverno, 2015;
92 Piana Agostinetti & Malinverno, 2010; Saygin et al., 2016). Its general advantage over
93 other approaches is that it produces parsimonious inference that results in better esti-
94 mates of uncertainties as shown in comparisons with more traditional fixed dimensional
95 inversions (Dettmer et al., 2016; Olugboji et al., 2017).

96 The most common parameterization used in these trans-dimensional inversions is
97 the Voronoi cell (Bodin & Sambridge, 2009; Burdick & Lekić, 2017; Galetti et al., 2016;
98 Saygin et al., 2016). When using Voronoi cells, a 2D or 3D region is parameterized as
99 a collection of cell centers with associated Earth model parameters. The number and lo-
100 cation of these nodes vary during the MCMC inversion. Predictions of the Earth model
101 values at a particular point in the domain correspond to the parameters of the nearest
102 node, hence Voronoi cells represent nearest neighbor polygons or polyhedra under an L_2
103 norm. A disadvantage of Voronoi cells is that they are not optimal for representing smoothly
104 varying functions. A second disadvantage is that the spatial gradient of the field is zero
105 everywhere except at the boundaries where spatial gradients are discontinuous. This pre-
106 vents their use in applications where the forward model requires spatial gradients or where
107 posterior inferences on spatial gradients are useful. Iterative approaches, whereby the
108 mean of a set of recent models in the Markov chain are used to generate smooth mod-
109 els from which approximations of spatial gradients can be obtained are possible, but add

110 further approximations. Conversely, an advantage of Voronoi cells is that they excel at
111 the discovery of spatial discontinuities.

112 Here we extend the Voronoi cell parameterization to Delaunay triangles with lin-
113 ear and cubic interpolants giving C^0 and C^1 continuous fields for 2D problems. These
114 extensions complement other extensions to Voronoi cell parameterizations such as the
115 Johnson—Mehl tessellation (Belhadj, Romary, Gesret, Noble, & Figliuzzu, 2018) and have
116 analogs in 1D trans-dimensional parameterizations used in geophysical problems where
117 “change points” are modelled with step functions (Ingham, Heslop, Roberts, Hawkins,
118 & Sambridge, 2014) or changes in gradient are modelled with piece wise linear functions
119 (Hopcroft, Gallagher, & Pain, 2007). We show that compared to the two alternatives,
120 the Voronoi cell parameterization poorly recovers features in the inversion of smooth mod-
121 els and introduces multi-modal posteriors that complicate the interpretation of uncer-
122 tainties. Conversely, the continuous parameterizations are able to better recover contin-
123 uous fields but perform poorly when attempting to fit observations based on underly-
124 ing discontinuous 2D fields.

125 Overall, we show that in cases where the estimated surface is likely to include dis-
126 continuities such as inference of tectonics from local GPS observations, a Voronoi cell
127 parameterization is likely to be preferable. For intrinsically smooth 2D fields such as tem-
128 perature, density, or gravity potentials, one of the new Delaunay parameterizations may
129 be more appropriate. The framework provided by this software allows this parameter-
130 ization choice which is important for optimal results, as espoused in recent 1D trans-dimensional
131 studies discussing parameterization trade-offs (Gao & Lekić, 2018; Roy & Romanowicz,
132 2017).

133 In a last section, we show a synthetic joint inversion of 3 different data sets to con-
134 strain relative sea level rise: tide gauge measurements, satellite altimetry and GPS ver-
135 tical land motion estimates. We jointly invert for two surfaces: absolute land motion,
136 and absolute sea level rise. This test further illustrates the fact that the choice of param-
137 eterization affects both the recovered structure and its estimated uncertainties as reported
138 by Hawkins and Sambridge (2015).

139 When used for 2D regression problems, our Bayesian trans-dimensional software
140 can be seen as an alternative to simple interpolation or kriging methods that generally
141 assume a constant spatial correlation length (Oliver & Webster, 1990). Our method is

142 more general and can include more complex forward modelling, likelihoods and error mod-
 143 els while adapting solutions to have finer resolution where observations are sufficiently
 144 informative.

145 The regression examples shown here are simple by design, yet the software allows
 146 arbitrary forward models and likelihood functions to be used and is therefore more widely
 147 applicable to geophysical problems and beyond. Some potential examples include the
 148 reconstruction of gravity anomalies from satellite measurements (Sandwell & Smith, 1997),
 149 reconstruction of the Moho discontinuity from geophysical data (Bodin, Salmon, et al.,
 150 2012), interpolation of aeromagnetic data (Billings, Beatson, & Newsam, 2002), and re-
 151 gional historic climate reconstructions (Hopcroft et al., 2009).

152 **2 Overview of the Algorithm**

153 **2.1 Parameterization**

154 We consider the inversion of geophysical data constrained to a 2D field, for exam-
 155 ple, a region on the Earth’s surface defined by latitude and longitude. We first introduce
 156 the three parameterizations considered, Voronoi cells, Delaunay triangulation with a lin-
 157 ear interpolant, and Delaunay triangulation with a Clough-Tocher interpolant. For each
 158 of the parameterizations, a model consists of a set of mobile 2D points (or nodes) with
 159 one or more Earth model parameters associated with each point.

160 The vector of unknown model parameters is thus defined as the set of geograph-
 161 ical locations and values associated to each node. Our three different parameterizations
 162 propose different ways to interpolate between nodes, and thus can be thought of as three
 163 different forward operators that generate a predicted surface from the vector of model
 164 parameters. Given a variable dimension model \mathbf{m} , for the forward model operator g can
 165 be written as $g = f \circ h$ where f is the user defined forward model and h is the param-
 166 eterization operator that maps the model vector into predictions in Cartesian space. The
 167 parameterization operator can be seamlessly be replaced by h_{Voronoi} , h_{Delaunay} or $h_{\text{Clough-Tocher}}$
 168 representing the 3 alternate parameterizations. Note that since the vector of model pa-
 169 rameters \mathbf{m} contains the position of nodes, which makes the operator g non-linear even
 170 in the cases presented here where the user forward model f is a linear regression oper-
 171 ator.

172 **2.1.1 Voronoi cells**

173 In the original introduction of the reversible jump approach of Green (1995), the
174 last example presented was an application of image segmentation using Voronoi cells. This
175 general algorithm has been extended to different geophysical problems such as resistiv-
176 ity tomography (Malinverno, 2002), seismic surface wave tomography (Bodin & Sam-
177 bridge, 2009), body wave tomography (Burdick & Lekić, 2017; Piana Agostinetti et al.,
178 2015), CSEM tomography (Ray & Key, 2012), finite fault inversion (Dettmer, Benavente,
179 Cummins, & Sambridge, 2014), estimates of coastal inundation (Choblet, Husson, & Bodin,
180 2014), and reconstructing surfaces of geodetic uplift rates (Husson, Bodin, Spada, Choblet,
181 & Comé, 2018).

182 In the Voronoi cell parameterization, the model is defined using a number of nodes
183 representing the Voronoi cell centers. Each Voronoi cell is given a set of one or more Earth
184 model parameters. The reconstructed surface parameter at a given point corresponds
185 to the value of the nearest Voronoi cell node. This parameterization produces surfaces
186 with constant values in each Voronoi cell and discontinuities at Voronoi cell edges.

187 The Voronoi cell approach would be seemingly implausible for the inversion of geo-
188 physical problems where heterogeneity is expected to be smooth. This seeming incon-
189 gruity hasn't prevented the successful application of trans-dimensional Voronoi cells to
190 geophysical inverse problems such as surface wave tomography inversion as the average
191 of a large ensemble of such models will generate a smoothly varying posterior mean (Bodin
192 & Sambridge, 2009; Galetti et al., 2016; Saygin et al., 2016).

193 **2.1.2 Delaunay triangulation with linear interpolation**

194 As an alternative, we propose a relatively simple modification to the Voronoi cell
195 approach where the dual of the Voronoi cell, the Delaunay triangulation is used. In this
196 parameterization, rather than the model nodes representing the center of Voronoi cells,
197 they represent vertices of a triangulation of the domain.

198 In this case, rather than the values at a given spatial point being determined by
199 a nearest node, the model nodes defining the triangle can be linearly interpolated to any
200 point within the triangle by computing Barycentric coordinates (Sambridge, Braun, &

201 McQueen, 1995). This then provides a model that describes a continuous field over the
 202 domain but with discontinuities in the gradient at triangle edges.

203 **2.1.3 Delaunay triangulation with Clough-Tocher interpolation**

204 A further extension to the Delaunay triangulation replaces the linear interpolant
 205 based on the barycentric coordinates of a point with a cubic interpolant, a modified Clough-
 206 Tocher interpolant (Clough & Tocher, 1965; Mann, 1998).

207 In this parameterization, gradients are estimated at nodes from the values at neigh-
 208 boring nodes, analogously to 1D Cubic Hermite interpolation. The estimated node gra-
 209 dients are subsequently used to constrain the normal gradients at triangle edges so that
 210 within each triangle, a cubic interpolant is available that also maintains continuous gra-
 211 dients across each triangle edge. There is an extra computation burden in this method
 212 as a small two by two system has to be solved for each node of the model before a point
 213 can be interpolated. Details of the exact formulation used here appear in supplementary
 214 material.

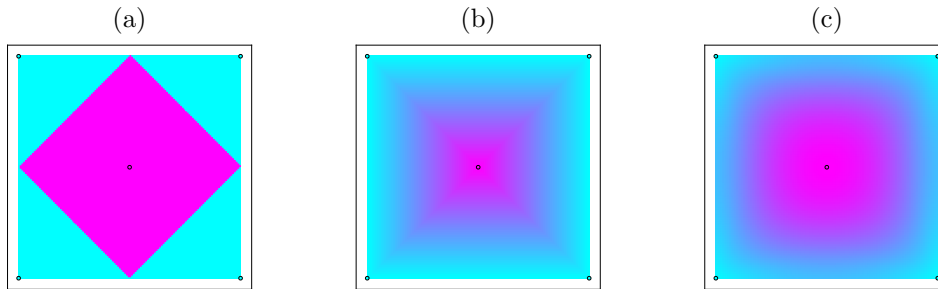
215 **2.1.4 Summary**

216 To give an example of each of the three parameterizations available in the software,
 217 in Figure 1 we show maps of a 2D field where the same model vector \mathbf{m} is used, defined
 218 with 5 nodes: one central node at (0,0) with a value of 1, and four corner nodes at $(\pm 1, \pm 1)$
 219 with values of 0, essentially a 2D delta function.

225 **2.2 Bayesian formulation**

226 In a Bayesian approach to inference, the solution we obtain is the *a posteriori* prob-
 227 ability distribution or posterior (Mosegaard & Tarantola, 1995; Sambridge & Mosegaard,
 228 2002). This is the probability density of the model space given the observed data, or writ-
 229 ten mathematically, $p(\mathbf{m}|\mathbf{d})$, where \mathbf{m} is our vector of model parameters and \mathbf{d} our vec-
 230 tor of observations. The posterior distribution is defined through Bayes' theorem (Bayes,
 231 1763)

$$p(\mathbf{m}|\mathbf{d}, \mathcal{I}) = \frac{p(\mathbf{m}|\mathcal{I})p(\mathbf{d}|\mathbf{m}, \mathcal{I})}{p(\mathbf{d}|\mathcal{I})}, \quad (2)$$



220 **Figure 1.** An example of the differences in each parameterization used in this study. Each
 221 of the parameterizations are defined with 5 points with a value of one at the center (0,0) and
 222 values of zero at the corners ($\pm 1, \pm 1$). In (a) is the Voronoi cell parameterization commonly used
 223 in trans-dimensional inversion, in (b) we show the linear Delaunay parameterization, and (c) the
 224 cubic Clough-Tocher parameterization.

232 where $p(\mathbf{m}|\mathcal{I})$ is the prior, $p(\mathbf{d}|\mathbf{m}, \mathcal{I})$ is the likelihood analogous to the measure of
 233 fit to the observations, and $p(\mathbf{d}|\mathcal{I})$ is normalization term often called the “evidence”. The
 234 dependence \mathcal{I} represents additional prior information within the formulation of problem
 235 and the chosen parameterization forms part of this dependence (Malinverno, 2002). In
 236 many non-linear geophysical inverse problems, this probability density function is ap-
 237 proximated numerically using MCMC techniques. As we will see in some synthetic ex-
 238 amples, the posterior is highly dependent on choices in the formulation of the problem
 239 with the focus herein on the selected parameterization.

240 In simple problems, the posterior can be evaluated analytically, but in many cases
 241 numerical methods are required. Markov chain Monte Carlo (MCMC) sampling approach
 242 can be applied to the numerator of the right-hand side of (2) to obtain an estimate of
 243 the posterior probability distribution up to the normalizing constant of the evidence, which
 244 is often difficult to compute explicitly (Sambridge, Gallagher, Jackson, & Rickwood, 2006),
 245 although numerical techniques are available (Brunetti, Linde, & Vrugt, 2017; Schöniger,
 246 Wöhling, Samaniego, & Nowak, 2014).

247 **2.3 Markov chain Monte Carlo (MCMC)**

248 In an MCMC inversion, an ensemble of plausible models is constructed, some of these
 249 models may not fit the observations optimally but nonetheless are representative of the
 250 tails or intermediate regions of multi-modal of posterior distributions. Models are included

251 in this ensemble based on a criteria for the acceptance of proposed perturbations to model
 252 parameters. A commonly used acceptance criterion is the Metropolis-Hastings (Hast-
 253 ings, 1970; Metropolis, Rosenbluth, Rosenbluth, Teller, & Teller, 1953) where for a pro-
 254 posed transition from model \mathbf{m} to \mathbf{m}' , the acceptance is given by

$$\alpha = \min \left\{ 1, \frac{p(\mathbf{m}'|\mathcal{I})}{p(\mathbf{m}|\mathcal{I})} \frac{p(\mathbf{d}|\mathbf{m}',\mathcal{I})}{p(\mathbf{d}|\mathbf{m},\mathcal{I})} \frac{Q(\mathbf{m}' \rightarrow \mathbf{m})}{Q(\mathbf{m} \rightarrow \mathbf{m}')} \right\}, \quad (3)$$

255 where the term $\frac{p(\mathbf{m}'|\mathcal{I})}{p(\mathbf{m}|\mathcal{I})}$ is the prior ratio, $\frac{p(\mathbf{d}|\mathbf{m}',\mathcal{I})}{p(\mathbf{d}|\mathbf{m},\mathcal{I})}$ the likelihood ratio, and $\frac{Q(\mathbf{m}' \rightarrow \mathbf{m})}{Q(\mathbf{m} \rightarrow \mathbf{m}')}$
 256 the proposal ratio.

257 The proposal ratio represents the probability distribution that perturbs an initial
 258 model \mathbf{m} to obtain \mathbf{m}' . At each iteration of an McMC inversion, a new model \mathbf{m}' is cre-
 259 ated, its likelihood computed and the acceptance rate calculated. The new model is ac-
 260 cepted with the probability α . If the new model is accepted, then \mathbf{m} is set to \mathbf{m}' , oth-
 261 erwise \mathbf{m}' is rejected and the current model is unchanged. After repeating this process
 262 for a suitably large number of iterations we obtain a set of models. It is customary to
 263 remove some number of initial models that are considered pre-converged or “burnin” mod-
 264 els, after which is left a chain or ensemble of models that approximate the posterior dis-
 265 tribution (Brooks, Gelman, Jones, & Meng, 2011).

266 2.4 Reversible Jumps

267 An extension to standard McMC is Birth/Death McMC (Geyer & Møller, 1994)
 268 and the more general Reversible Jump McMC (Denison et al., 2002; Green, 1995; Ma-
 269 linverno, 2002) where additional proposals are available that change the model dimen-
 270 sion, that is, the number of Voronoi nodes or Delaunay vertices in our case. The accep-
 271 tance criteria for reversible jump or trans-dimensional steps is

$$\alpha = \min \left\{ 1, \frac{p(\mathbf{m}'|\mathcal{I})}{p(\mathbf{m}|\mathcal{I})} \frac{p(\mathbf{d}|\mathbf{m}',\mathcal{I})}{p(\mathbf{d}|\mathbf{m},\mathcal{I})} \frac{Q(\mathbf{m}' \rightarrow \mathbf{m})}{Q(\mathbf{m} \rightarrow \mathbf{m}')} |\mathcal{J}| \right\}, \quad (4)$$

272 where the additional term $|\mathcal{J}|$ is the determinant of the Jacobian of the model trans-
 273 formation from one dimension or parameterization to another. This is required to pre-
 274 serve volume between the two dimensions.

275 In the context of the parameterizations discussed here, trans-dimensional steps change
276 the number of nodes used to fit the observations. This is facilitated with proposals that
277 add and remove a single nodal point and its associated parameter values, called Birth
278 and Death proposals (Geyer & Møller, 1994). The number and distribution of nodes self-
279 adapts to the resolving power of the data, which is in stark contrast to traditional meth-
280 ods that impose a globally fixed resolution in the formulation of the problem, that is,
281 through a fixed grid.

282 **2.5 Hamiltonian Monte Carlo**

283 Through the careful tuning of proposal distributions, the acceptance rates of McMC
284 inversion can approach optimal values. One inherent problem with McMC is that pro-
285 posals are generally designed to be small perturbations from the current model, for ex-
286 ample, perturbations sampled from a Gaussian distribution. The size of the perturba-
287 tions need to be tuned to be small to achieve reasonable acceptance rates and as such
288 can result in a high degree of correlation between neighboring models in a chain. This
289 reduces the effectiveness of the chain to estimate the posterior by reducing the Effective
290 Sample Size (ESS) (Brooks et al., 2011).

291 An advance over McMC is Hamiltonian Monte Carlo (Duane, Kennedy, Pendel-
292 ton, & Roweth, 1987; Neal, 1994, 2011) (originally called Hybrid Monte Carlo), where
293 an additional calculation of the gradient of the likelihood function is used to propose mod-
294 els that are less correlated, that is, further away from the current model while retain-
295 ing a high likelihood and higher probability of acceptance. Hamiltonian Monte Carlo in-
296 creases convergence rates and increases the effective sample size of a chain resulting in
297 fewer iterations required for sampling a posterior. This comes at the expense of requir-
298 ing calculation of gradients. Regardless of this extra cost, Hamiltonian Monte Carlo has
299 recently been used in some non-linear geophysical inverse problems (Fichtner & Simutè,
300 2018; Fichtner, Zunini, & Gebraad, 2019; Sen & Biswas, 2017).

301 Both the more common Metropolis-Hastings McMC and HMC build an ensemble
302 of plausible models through a Markov chain and are hence Markov chain methods. The
303 primary difference that in McMC we sample and apply a perturbation to the current model
304 from a probability distribution. In HMC, a random initial momentum is sampled and

305 the model trajectory is simulated with Hamiltonian dynamics using the log of the pos-
 306 terior as the potential in the Hamiltonian equation.

307 In the problem considered in this paper, the model parameters consist of a set of
 308 node positions and their associated values. Since the existence of the gradient of the like-
 309 lihood with respect to node positions is forward model dependent for the Voronoi cell
 310 parameterization, we use Metropolis-Hastings proposals for perturbing the location of
 311 nodes, Hamiltonian proposals perturbing the values associated with nodes and reversible
 312 jump proposals for changes of dimension although hybrid HMC/reversible jump propos-
 313 als are possible (Sen & Biswas, 2017).

314 2.6 Likelihood and Hierarchical error estimation

315 The form of a likelihood function in an inverse problem in a Bayesian framework
 316 is primarily dictated by the expected distribution of errors in the formulation of the in-
 317 verse problem with contributions from the data errors and forward modelling errors. The
 318 common assumption is that

$$\mathbf{d}_{\text{observed}} = g(\mathbf{m}_{\text{true}}) + \epsilon_{\text{data}} + \epsilon_{\text{theory}} + \epsilon_{\dots}, \quad (5)$$

319 that is, our observations are a sum of the observations predicted from the true model
 320 plus some combination of known and unknown sources of errors. Here we have indicated
 321 two common sources of noise, ϵ_{data} represents measurement or observational errors, and
 322 ϵ_{theory} represents general theoretical errors that include simplifying approximations and
 323 numerical imprecision in forward modelling represented by the operator g , but also er-
 324 rors due to the inability of the parameterization to represent the true 2D field.

325 The likelihood for a particular set of predictions from a model, $g(\mathbf{m})$, becomes

$$p(\epsilon) = p(g(\mathbf{m}) - \mathbf{d}), \quad (6)$$

326 where ϵ without the subscript represents the combined noise.

327 A common choice of likelihood function is a Gaussian distribution. The rationale
 328 for this is that since we assume that the noise ϵ is a combination of various sources of

329 error, the resulting distribution will be asymptotically Gaussian due to the central limit
 330 theorem (assuming the errors have finite variance).

331 A Gaussian likelihood is of the form

$$p(\mathbf{m}|\mathbf{d}, \mathcal{I}) = \frac{1}{\sqrt{2\pi}|C_d|} \exp \left\{ -\frac{1}{2} (g(\mathbf{m}) - \mathbf{d})^T C_d^{-1} (g(\mathbf{m}) - \mathbf{d}) \right\}, \quad (7)$$

332 where C_d is the covariance matrix of errors. The software allows writing of custom
 333 likelihood functions, however for simplicity we are using diagonal covariance matrices,
 334 that is, the errors are independent for each observation. In more complex and real data
 335 problems, this assumption would be overly simplistic and covariance or auto regressive
 336 errors would be more appropriate (Bodin, Sambridge, et al., 2012; Dettmer et al., 2012;
 337 Dosso & Wilmut, 2006; Kolb & Lekić, 2014). In the diagonal covariance matrix case, the
 338 Gaussian likelihood reduces to

$$p(\mathbf{m}|\mathbf{d}, \mathcal{I}) = \frac{1}{\prod_i \sqrt{2\pi}\sigma_i} \exp \left\{ -\sum_i \frac{(g(\mathbf{m})_i - \mathbf{d}_i)^2}{2\sigma_i^2} \right\}. \quad (8)$$

339 The observational uncertainty is often estimated crudely in real world applications
 340 and will not account for other sources of error such as theoretical errors. This suggests
 341 that given

$$\epsilon = \epsilon_{\text{data}} + \epsilon_{\text{theory}} + \dots, \quad (9)$$

342 that the σ value in (8) should in fact be set to

$$\sigma_i = \sqrt{\sigma_{i,\text{observation}}^2 + \sigma_{\text{theory}}^2} \quad (10)$$

343 where σ_{theory} is the unknown standard deviation of the theoretical noise. This un-
 344 known theoretical noise can be included as a hyper-parameter to be inverted for during
 345 the inversion using a hierarchical Bayes approach (Malinverno & Briggs, 2004).

346 Formulating a hierarchical error model is a complex procedure, and while the soft-
 347 ware supports an arbitrary number of hierarchical parameters, we have elected to assume
 348 that the theoretical errors are small relative to the data errors and use a single scaling
 349 term, that is

$$\sigma_i = \lambda \sigma_{i,\text{observation}}, \quad (11)$$

350 where λ is the unknown scaling term. The benefit of this approach, in addition to
 351 its simplicity, is that it preserves the relative weighting of the inversion due to individ-
 352 ual observational errors. In real data problems, such a simple hierarchical error model
 353 may not be appropriate. Again we stress that this is implemented in the user defined
 354 likelihood function and so the operation of hierarchical parameters can be modified to
 355 suit problems where the above assumptions are not appropriate.

356 2.7 Parallel Tempering

357 One of the common issues with trans-dimensional sampling is the often low accep-
 358 tance rates for trans-dimensional proposals resulting in poor sampling of the posterior,
 359 which is particularly important for statistical inference on the number of parameters. While
 360 various approaches have been successfully applied to improve the acceptance rates of trans-
 361 dimensional proposals (Al-Awadhi, Hurn, & Jennison, 2004; Sen & Biswas, 2017), we in-
 362 corporate Parallel Tempering (Dosso, Holland, & Sambridge, 2012; Earl & Deem, 2005;
 363 Sambridge, 2014) in the inversion to improve mixing between models with different di-
 364 mensions.

365 Parallel Tempering uses multiple parallel chains at different temperatures T , with
 366 statistical inference performed only with the chains at $T = 1$. The effect of the tem-
 367 perature is in the acceptance criteria where it is applied to the likelihood ratio

$$\alpha = \min \left\{ 1, \frac{p(\mathbf{m}'|\mathcal{I})}{p(\mathbf{m}|\mathcal{I})} \left[\frac{p(\mathbf{d}|\mathbf{m}',\mathcal{I})}{p(\mathbf{d}|\mathbf{m},\mathcal{I})} \right]^{1/T} \frac{Q(\mathbf{m}' \rightarrow \mathbf{m})}{Q(\mathbf{m} \rightarrow \mathbf{m}')|\mathcal{J}|} \right\}, \quad (12)$$

368 where T is the temperature. At higher temperature, the effect of the likelihood ra-
 369 tio is diminished and the trans-dimensional proposals acceptance rates will tend to in-
 370 crease. Periodically, model exchanges are proposed between chains at different temper-
 371 atures enabling better exploration of the posterior and mixing between models of dif-
 372 ferent dimension.

373 2.8 Convergence

374 In an McMC/HMC simulation, a large number of candidate models are available
 375 from which statistical inference can be made. It is common practice to remove some num-
 376 ber of models from the start of the chain, called “burn in” samples where the chain may
 377 contain unconverged models. In addition, chain thinning is often performed where only
 378 every n th model is retained from the chain to reduce the effect of correlation between
 379 neighboring models in the chain. While we utilize HMC to reduce this correlation po-
 380 tentially obviating the need for thinning, we retain McMC proposals for moves of type
 381 birth, death and hierarchical proposals, i.e. perturbations to λ in (11).

382 To ensure convergence within a trans-dimensional inversion, standard approaches
 383 such as the Gelman-Rubin statistic (Gelman & Rubin, 1992) are difficult to apply as the
 384 variance of an individual model parameters cannot be reliably calculated in a chain where
 385 the model dimension changes. The Gelman-Rubin statistic can be computed for hyper-
 386 parameters of the inversion such as the hierarchical error scale which does give some mea-
 387 sure of the convergence between chains (Hawkins et al., 2017).

388 2.9 Summary

389 In the algorithm presented here, we simulate multiple Markov chains initialized with
 390 from random models using independently seeded random number generators. The chain
 391 is simulated for a fixed number of iterations and at each iteration, one of the following
 392 proposals is chosen at random

393 **Value** The value(s) of the nodes are perturbed using a Hamiltonian Monte Carlo pro-
 394 posal.

395 **Move** The position of a randomly chosen node is perturbed using an McMC proposal.

396 **Birth** A new node and its associated value(s) are added using an rjMcMC proposal.

397 **Death** A node is selected at random to be removed using an rjMcMC proposal.

398 **Hierarchical** The hierarchical scaling parameter is perturbed using an McMC proposal.

399 During the inversion and at a predefined rate, the independent chains perform a
 400 parallel tempering exchange swap. Only the chains with temperatures of one have their
 401 ensembles processed for statistical inferences. Details of each class of the proposal ap-
 402 pear in appendices.

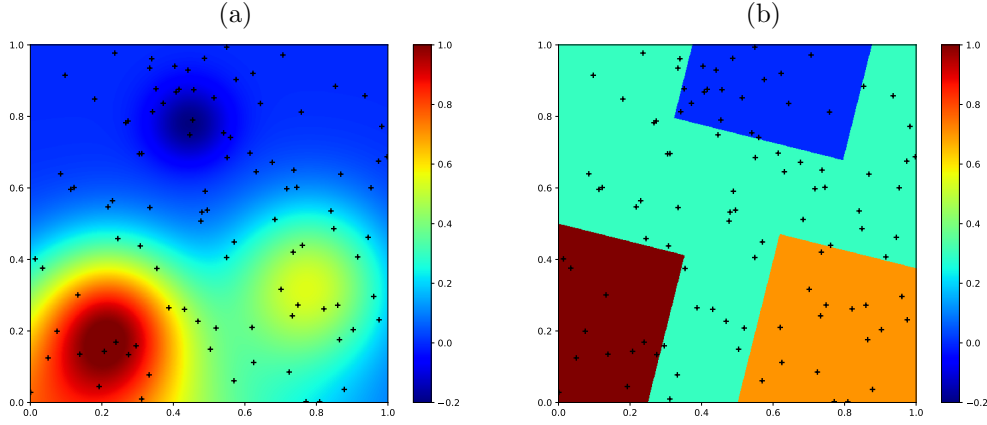
3 Synthetic Regression

As a first demonstration of the software and the effects of parameterization, we present an application to a 2D regression problem. We show that the posterior solution (and hence estimated surface uncertainties) strongly depends on the parameterization. The main point here is to demonstrate the effects of a poor parameterization choice. The first surface to reconstruct is shown in Figure 2(a), it is smooth and consists of the sum of four Gaussians. The second, shown in Figure 2(b) is a tessellated image with regions approximately corresponding to the first, but with straight edged discontinuities.

The synthetic observations were created by randomly generating 100 points within the region, illustrated with crosses in the figures, and sampling the true model at those points. Independent Gaussian noise was added to each observation with a standard deviation of 0.05, which is approximately a five percent error level given the range of values is approximately $0 \dots 1$.

In total six inversions are computed using the three different parameterizations and the two synthetic data sets. The same settings were used for each inversion, that is, we use 28 parallel chains with 4 temperatures logarithmically spaced between 1 and 5. The initial model is randomly generated from the priors. The Hamiltonian step size and McMC proposal widths are tuned to obtained reasonable acceptance rates (approximately 0.80 for HMC and 0.24 for McMC). The prior on the values are set to uniform between -0.5 and 2, thus encompassing the range of the unknown Earth model parameter in this synthetic example. The prior on the hierarchical scaling is also uniform between 0.5 and 5. Each inversion was simulated for one million iterations.

In Figure 3 we show the results for the inversion of the synthetic regression data set created from the smooth model. In this case, for summary purposes, we have chosen to show the mean and standard deviation of the ensemble, however other choices are possible such as median and credible interval widths (we show images of absolute errors from the true model and maximum a posteriori probability (MAP) images in the supplementary material). In each case, the true model is recovered relatively well given the level of noise. In the mean models, the progressively smoother results are evident as higher order interpolants are used, that is in (a) Voronoi cells are effectively 0th order, followed in (c) by Delaunay with a linear interpolant and lastly in (e) Delaunay with a cubic interpolant.

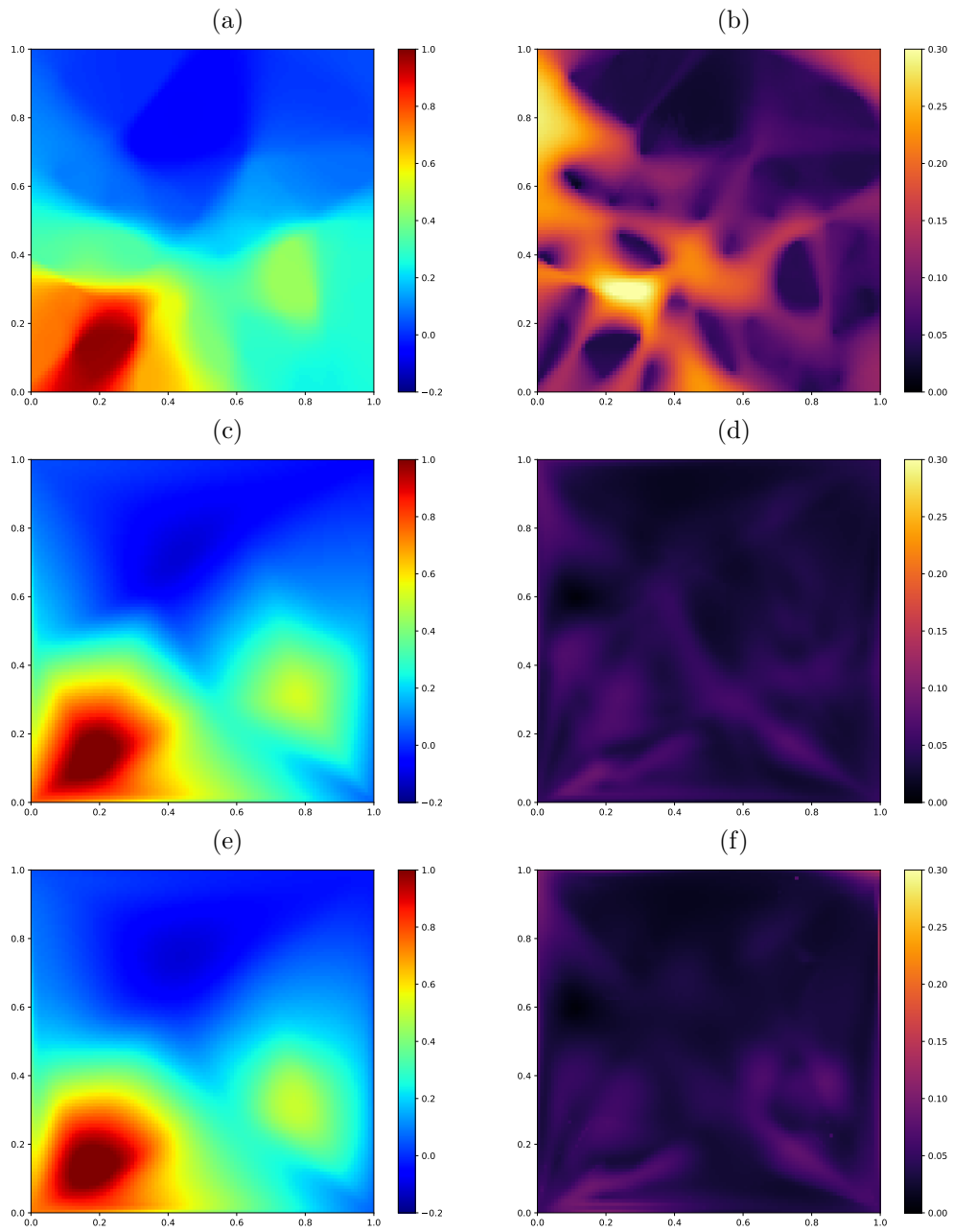


425 **Figure 2.** The true models used in the synthetic regression examples. In (a) the true model is
 426 smooth and consists of a sum of four Gaussians, whereas (b) is a tessellated approximation of the
 427 same model with straight edges and discontinuities. The randomly located observation points are
 428 indicated with crosses.

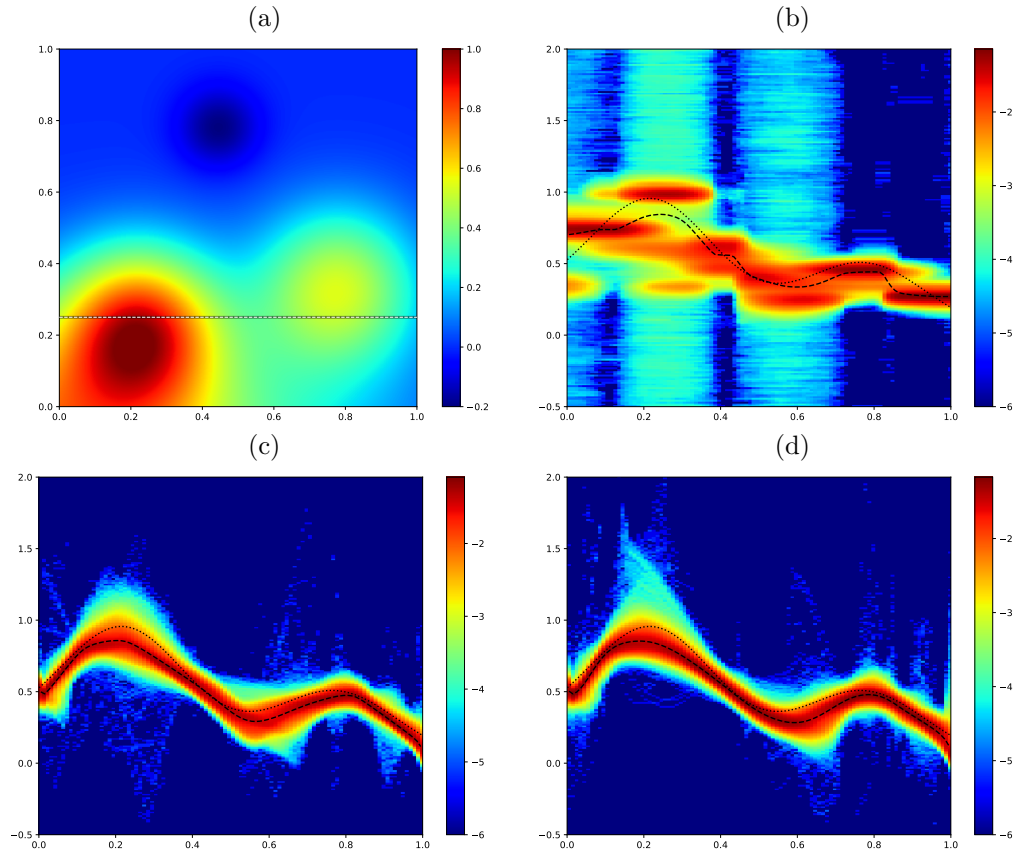
444 The standard deviation maps of the Voronoi cell parameterization in Figure 3(b)
 445 contain ring like structures. These features are caused by the combination of disconti-
 446 nuities in the Voronoi cell parameterization and their mobility. It has been claimed that
 447 this feature is only evident in non-linear forward models such as non-linear tomography
 448 (Galetti, Curtis, Meles, & Baptie, 2015), however we see they appear here in a linear re-
 449 gression forward model.

450 Trans-dimensional inversion with Voronoi cells introduces non-linearity to the prob-
 451 lem through the dynamic number and location of Voronoi nodes. Strictly speaking, these
 452 filaments of large standard deviation occur due to the mobility of the Voronoi cells in-
 453 troducing multi-modalities in the posterior near Voronoi cell edges, which in turn leads
 454 to large standard deviations. We can see that the posterior standard deviation for the
 455 two Delaunay parameterizations by comparison are generally smaller.

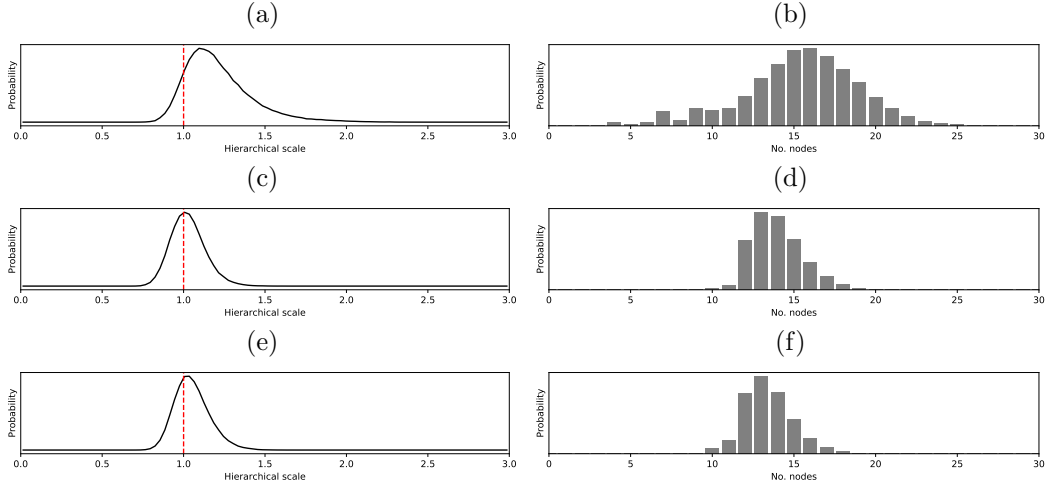
462 In trans-dimensional inversion, and particularly for Voronoi cell parameterizations,
 463 simply plotting the standard deviation as a measure of uncertainty will not necessarily
 464 give an accurate appraisal of the posterior. If we instead take a transect through the en-
 465 semble along a particular horizontal line and look at the marginal probability distribu-
 466 tions, we can visibly see how the distribution varies spatially. In Figure 4 we show the
 467 distribution along a horizontal transect for each of the parameterizations in (b), (c) and
 468 (d) with the location of the transect indicated with a dashed line in (a). What is clear



439 **Figure 3.** The summary plots for the inversion of the smooth model. In (a) and (b) are the
 440 mean and standard deviation results for the Voronoi cell parameterization. In (c) and (d) are
 441 the mean and standard deviation results for the Delaunay triangulation with linear interpolant
 442 parameterization. In (e) and (f) are the mean and standard deviation results for the Delaunay
 443 triangulation with Clough-Tocher interpolant.



456 **Figure 4.** In (a) we show the location of a transect taken through the ensemble to show dis-
 457 tribution of models. In (b) we show the distribution for the Voronoi cell parameterization, in (c)
 458 the Delaunay parameterization with linear interpolation, and (d) the Delaunay parameterization
 459 with Clough-Tocher interpolation. In each of the distribution plots, we show the \log_{10} of the
 460 probability, the ensemble mean is plotted with a dashed line, and the true model with a dotted
 461 line.



477 **Figure 5.** Posterior histograms from the inversion of the smooth data set for the hierarchical
 478 scaling factor are shown in (a) for the Voronoi parameterization, (c) for the Linear Delaunay
 479 parameterization and (e) for the Clough-Tocher Delaunay parameterization. Histograms for the
 480 number of model nodes are similarly shown in (b), (d) and (f) for the three parameterizations.
 481 The two Delaunay parameterizations in this case have hierarchical scaling factors close to one,
 482 and fewer number of model parameters.

469 is that the Voronoi cell parameterization has several regions where the distribution is multi-
 470 modal. For example, taking a vertical line at approximately $y = 0.25$ in Figure 4(b)
 471 would produce four peaks. Computing the standard deviation of such a multi-modal dis-
 472 tribution would produce large values, and this is the underlying cause of the large mag-
 473 nitude standard deviations seen in Figure 3(b). Even though the Voronoi cell parame-
 474 terization is a zeroth order discontinuous parameterization, from Figure 4(b) we can see
 475 that the ensemble mean (black dashed line) of the Voronoi model is smooth and reason-
 476 ably approximates the true model (black dotted line).

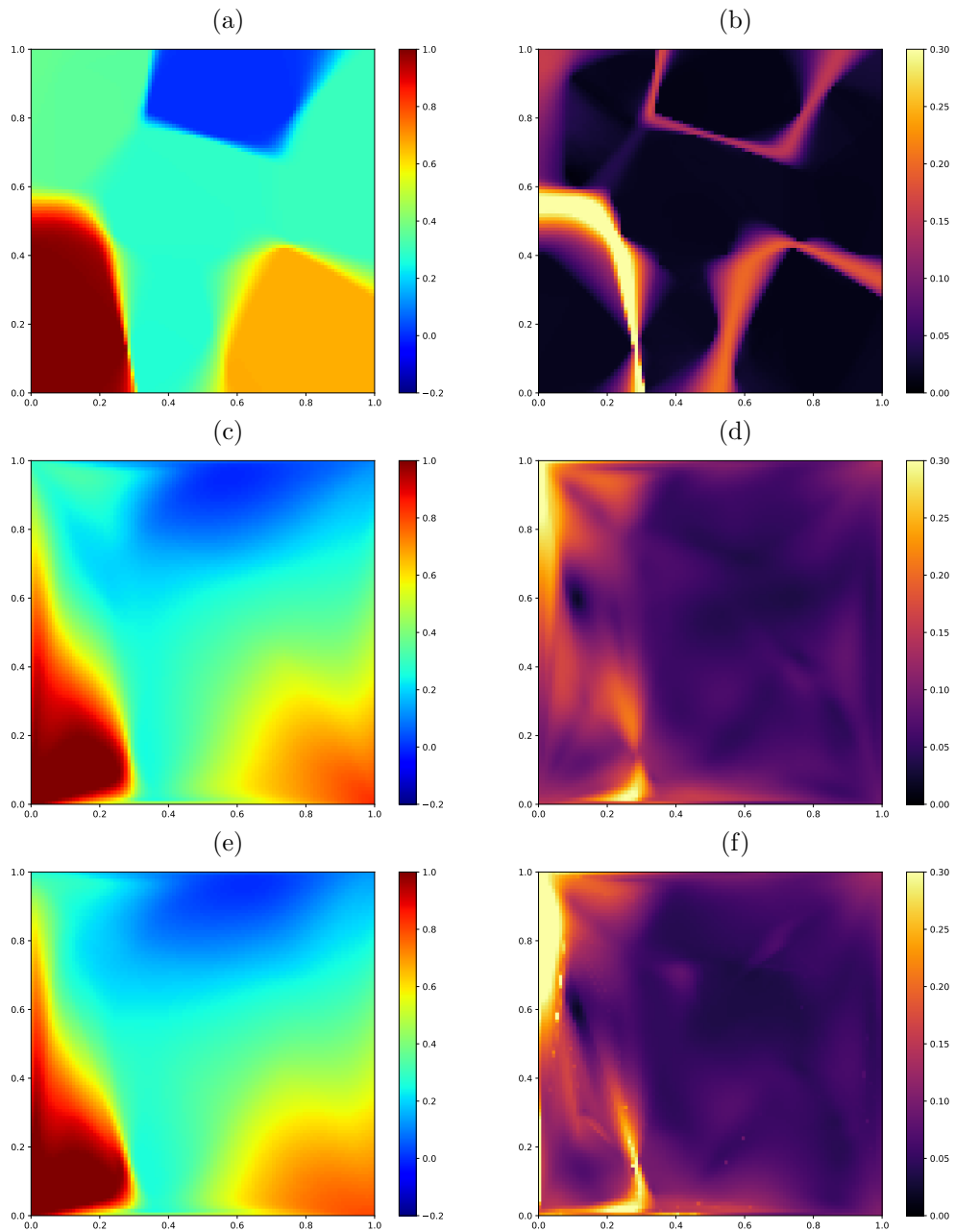
483 Given the Voronoi parameterization is poor at representing a smooth Gaussian field,
 484 we should expect higher levels estimated for the hierarchical error scale in the Voronoi
 485 parameterization than for the Delaunay parameterizations. Recall that the level of es-
 486 timated error given by the hierarchical parameter can be seen as the level of data fit achieved
 487 by the model and its parameterization. In Figure 5 we show the histograms of the num-
 488 ber of nodes for all chains combined with the hierarchical scaling parameters for each
 489 of the inversions in (a), (c), and (e). Since this inversion is for a synthetic experiment
 490 where we know the true noise level, the hierarchical error scale should converge to ap-

491 proximately one when the parameterization is able to predict the observations to within
492 noise level.

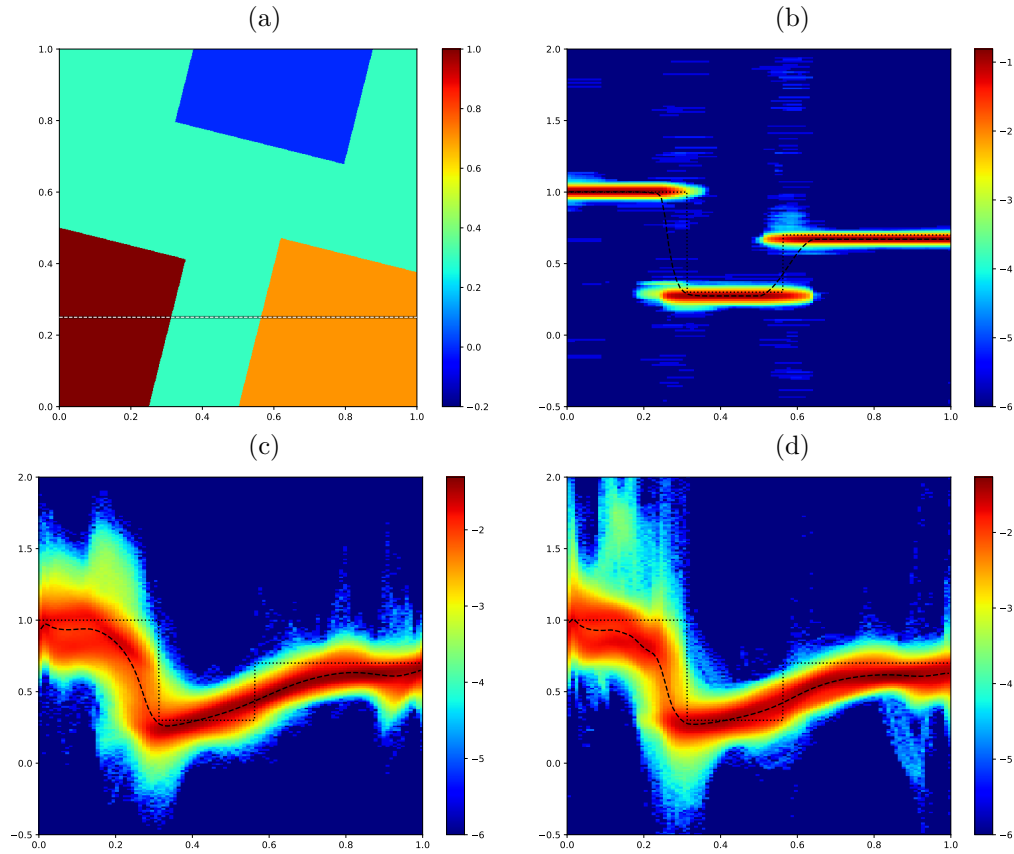
493 From the plots we can see that both the Delaunay parameterizations have histograms
494 with modes of approximately one, whereas the Voronoi parameterization has a slightly
495 higher mode and a longer tail. Also in Figure 5 we show the posterior histogram on the
496 number of model nodes in (b), (d) and (f). We observe that the mean and the variance
497 of the distribution is larger for Voronoi cells (b) than for Delaunay parameterization (d
498 and f). Overall, the Voronoi parameterization uses more cells and produce a worse data
499 fit than Delaunay parameterizations. Since the theoretical errors introduced by the poor
500 parameterization choice of Voronoi cells in this case is non-zero, the hierarchical estimate
501 of the error scaling term is greater than one.

507 In Figure 6 we show results for the inversion of of observation obtained from the
508 discontinuous 2D field shown in Figure 2(b). Here the Voronoi cell parameterization has
509 better recovered the true field than the two Delaunay parameterizations which only pro-
510 duce smooth approximations of the truth.

511 In this case, the standard deviation for the Voronoi cell parameterization has large
512 values coincident with the the discontinuities in the 2D field. This is not surprising as
513 the edges are not precisely constrained by the observations leading to uncertainty in their
514 location which in turn will lead to a multi-modal posterior distribution proximate to true
515 edges. As stated for the previous inversions, computing the standard deviation of a multi-
516 modal distribution will naturally lead to a large uncertainties as shown in these results.
517 Some authors (Burdick & Lekić, 2017; Cho, Gibson, & Zhu, 2018; Olugboji et al., 2017)
518 have suggested that areas of large uncertainties can be used as a proxy of the location
519 of discontinuities with models. In this synthetic example, it would appear that this in
520 indeed a reliable proxy for the location of discontinuities, however compare this to the
521 results for the smooth model in Figure 3(b) where we have similar large standard devi-
522 ations in the inversion of a continuous model. Discontinuities in an underlying 2D field
523 will lead to large standard deviations in the posterior, but large standard deviations do
524 not necessarily imply discontinuities. It is a characteristic of Voronoi cell trans-dimensional
525 inversion with mobile cells that they produce regions of multi-modal posteriors leading
526 to ring like structures of large magnitude in maps of posterior standard deviation.



502 **Figure 6.** The summary plots for the inversion of the tessellated model. In (a) and (b) are
 503 the mean and standard deviation results for the Voronoi cell parameterization. In (c) and (d) are
 504 the mean and standard deviation results for the Delaunay triangulation with linear interpolant
 505 parameterization. In (e) and (f) are the mean and standard deviation results for the Delaunay
 506 triangulation with Clough-Tocher interpolant.



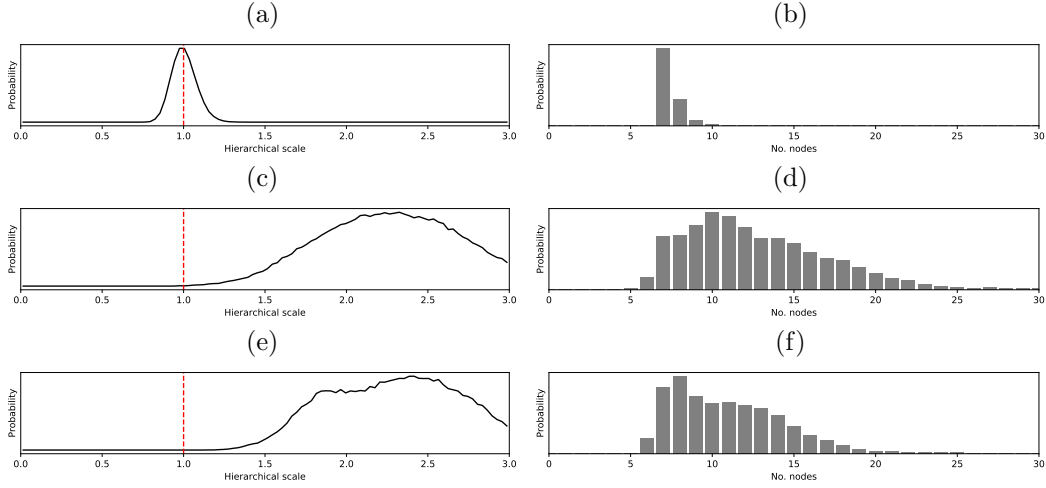
527 **Figure 7.** In (a) we show the location of a transect taken through the ensemble to show distri-
 528 bution of models. In (b) we show the distribution for the Voronoi cell parameterization, in (c)
 529 the Delaunay parameterization with linear interpolation, and (d) the Delaunay parameterization
 530 with Clough-Tocher interpolation. In each of the distribution plots, we show the \log_{10} of the
 531 probability, the ensemble mean is plotted with a dashed line, and the true model with a dotted
 532 line.

533 Once again in Figure 7 we show the posterior estimates of the reconstructed sur-
534 face. In this inversion we can clearly see that the posterior for the Voronoi cell param-
535 eterization has very narrow posterior widths. The cause of the large standard deviations
536 near discontinuities in the 2D field in Figure 6(b) can be clearly seen in this Figure 7(b)
537 where the posterior is strongly bi-modal near discontinuities due to uncertainty in the
538 location of discontinuities.

539 Both the Delaunay triangulation parameterizations have approximated the discon-
540 tinuous model with a smooth function. Due to the poor ability of the parameterization
541 to represent the true discontinuous surface, the uncertainties are much broader. It should
542 be noted here that even though the mean model with the two Delaunay parameteriza-
543 tions may be a poor representation of the true discontinuous surface, the true model re-
544 mains well within the higher probability region of the posterior. This is an important
545 result: even in the case of a poorly chosen parameterization, the algorithm is able to ad-
546 just both the model complexity (number of nodes) and data uncertainty (through the
547 scaling parameter λ) and to provide accurate surface uncertainties. If the parameteri-
548 zation choice is poor, there will be a corresponding increase in the estimated level of data
549 errors (due to increased theory errors), which will be reflected in higher uncertainties in
550 posterior estimates of the 2D field.

557 In Figure 8, for each of the inversions, we show posterior distribution for the hi-
558 erarchical error scale parameter in (a), (c), and (e) and for the number of nodes in (b),
559 (d) and (f). We can see that the Voronoi parameterization has fit the observations well
560 to the level of added noise with the mode of the hierarchical scale posterior approximately
561 one and relatively tightly constrained. In contrast, the hierarchical scale posteriors for
562 the two Delaunay parameterizations have much larger modes and are more weakly con-
563 strained. A similar trend is observed in (b), (d) and (f) where we show the posterior his-
564 togram on the number of model nodes. The recovery of the noise level in the Voronoi
565 cell parameterization here can generally only be achieved in synthetic tests where we know
566 the noise model. In a real world problem where the true noise and forward modelling
567 is more complex, such a tightly constrained result as in the Voronoi cell parameteriza-
568 tion may not be possible due to approximations in the hierarchical error model.

569 Given this new general software framework for constraining 2D fields with a con-
570 figurable parameterization, an obvious question arises as to which parameterization should



551 **Figure 8.** Posterior histograms from the inversion of the tessellated data set for the hierarchi-
 552 cal scaling factor are shown in (a) for the Voronoi parameterization, (c) for the Linear Delaunay
 553 parameterization and (e) for the Clough-Tocher Delaunay parameterization. Histograms for the
 554 number of model nodes are similarly shown in (b), (d) and (f) for the three parameterizations. In
 555 this case, the Voronoi parameterization recovers the true level of noise and uses fewer parameters
 556 than the two Delaunay parameterizations.

571 be used. Many approximate criteria exist for model choice problems, however most as-
 572 sume a fixed number of parameters (Akaike, 1974; Schwarz, 1978). These criteria pro-
 573 vide an approximation of Bayes factors or evidence ratios that can be used to select which
 574 model best fits our observations. The Deviance Information Criteria (DIC) has the ad-
 575 vantage that it can be applied in trans-dimensional inversion (Hawkins & Sambridge,
 576 2015; Steininger, Dosso, Holland, & Dettmer, 2014). The DIC variant we use for trans-
 577 dimensional inversions is given by

$$\text{DIC} = \overline{D(\mathbf{m})} + \frac{1}{2} \text{var}(D(\mathbf{m})), \quad (13)$$

578 where $D(\mathbf{m})$ is called the deviance and given by

$$D(\mathbf{m}) = -2 \log p(\mathbf{m}|\mathbf{d}, \mathcal{I}) + \text{constant}, \quad (14)$$

579 where the constant is a function of the data and cancels for model comparison pur-
 580 poses. Here the mean and variance refer to the posterior expectations of the deviance
 581 which can be approximated from the Markov chain ensemble. The mean of the deviance

582 gives a measure of the fit to the observations, where as its variance penalizes over pa-
 583 rameterization as an over parameterized model leads to higher degrees of freedom and
 584 hence larger variance in the posterior deviance.

585 The attraction of this criteria is its simplicity to compute as we only need to cal-
 586 culate the mean and standard deviation of the ensemble negative log likelihoods. Many
 587 other criteria such as the AIC and BIC require the calculation of the maximum likeli-
 588 hood and the number of model parameters. In a trans-dimensional inversion, the num-
 589 ber of model parameters is dynamic, with the maximum likelihood model likely belong-
 590 ing to an over-parameterization model within the ensemble.

591 In Table 1 we show the DICs computed for each of the parameterizations for the
 592 two inversions. We can see that in the inversion of the true smooth model, the two De-
 593 launay parameterizations are significantly preferred to the Voronoi cell model. It is some-
 594 what surprising that the Clough-Tocher parameterization is not preferred, however the
 595 difference between the Linear and Clough-Tocher Delaunay parameterization is small.
 596 For the tessellated true model, the preferences are reversed as expected. Before closing
 597 here, we again stress that the DIC is an approximate model comparison and is not with-
 598 out its limitations and criticisms. From a Bayesian perspective, the best approach for
 599 determining the support of one parameterization over the other is through computing
 600 Bayes factors (Kass & Raftery, 1995) which requires computation of the evidence which
 601 may be a future extension of this software.

606 **4 Synthetic case study: relative sea level, absolute sea level and ver-** 607 **tical land motion**

608 As a further synthetic example, we now illustrate the potential of the software on
 609 a geophysical inverse problem involving three sets of disparate observations. The goal
 610 here is to estimate the relative sea level rise from a combination of tide gauges, satel-
 611 lite altimetry and GPS vertical land motion estimates. This problem involves reconstruct-
 612 ing different surfaces that are either continuous and smoothly varying (absolute sea level),
 613 or have discrete transitions or sharp spatial gradients (vertical land motion). We there-
 614 fore use this joint inversion as a canonical example, but many alternatives exists both
 615 within geophysics and other fields.

(a)

Parameterization	$\overline{D(\mathbf{m})}$	$\text{var}(D(\mathbf{m}))$	DIC
Voronoi	-481.130	820.787	-70.736
Delaunay	-512.471	211.326	-406.808
Clough Tocher	-507.714	205.422	-405.003

(b)

Parameterization	$\overline{D(\mathbf{m})}$	$\text{var}(D(\mathbf{m}))$	DIC
Voronoi	-516.945	23.317	-505.286
Delaunay	-355.045	1411.684	350.797
Clough Tocher	-352.460	1175.300	235.190

602 **Table 1.** The DIC values computed for each of the parameterizations for the inversion of the
603 smooth and tessellated synthetic data. The lowest DIC value is the preferred model. In (a) for
604 the smooth synthetic data, the Linear Delaunay parameterization is preferred whereas in (b) for
605 the tessellated synthetic data the Voronoi parameterization is preferred.

616 Understanding sea level rise due to anthropogenic global warming has important
617 ramifications for coastal communities which contain a large proportion of the world’s pop-
618 ulation. The rates at which sea level currently changes along the coastline is determined
619 by the local vertical land motion (mostly due to post-glacial isostatic rebound) and global
620 sea level rise, due predominantly to melting glaciers and thermal expansion of the oceans
621 (Cazenave & Cozannet, 2013; Church & White, 2011).

622 Tide gauges observing the sea level over long time periods are used for the direct
623 measurement of relative sea level rates. However, tide gauges are subject to bias caused
624 by man-made and natural local changes to coastlines, and by instrumental measurement
625 errors. Their time series often have large uncertainties and associated record lengths strongly
626 vary among stations. Deriving a comprehensive view of relative sea level change solely
627 from tide gauges is therefore challenging.

628 While tide gauges measure directly the relative sea level rate, that is, the differ-
629 ence between absolute rates of sea level rise and vertical land motion, rates of absolute

630 sea level have been accurately measured globally using satellite based microwave radar
 631 altimetry since 1992 (from the launch of Topex/Poseidon, followed by Jason 1 and Ja-
 632 son 2). However, while absolute sea level measurement from satellites are accurate in the
 633 open ocean, they are problematic near shorelines due to spurious signals from land re-
 634 flections (Gommenginger et al., 2011). On land, the deployment of GNSS stations around
 635 the globe for measuring rates of vertical land motion (in addition to lateral movement)
 636 provide good constraints on recent rates of vertical land motion with a generally denser
 637 coverage than tide gauges (Blewitt, Kreemer, Hammond, & Gazeaux, 2015).

638 Previously, trans-dimensional Voronoi cells have been used to create maps of rel-
 639 ative sea level rise directly from tide gauge observations (Choblet et al., 2014) and for
 640 estimating Glacial Isostatic Adjustment (GIA) from vertical land motion as inferred from
 641 GNSS (Global Navigation Satellite System) stations (Husson et al., 2018).

642 Here we propose a synthetic inversion to jointly construct maps of absolute sea level
 643 rise and vertical land motion from which relative sea level rise and therefore coastal in-
 644 undation can be inferred, similar to previous regional studies that instead evaluated time
 645 series locally (Pfeffer & Allemand, 2016; Pfeffer, Spada, Mémin, Boy, & Allemand, 2017).

646 A distinction between this sea-level example and the previous theoretical example
 647 is that here we parameterize two independent 2D fields, one to represent the rate of ab-
 648 solute sea level rise, and the other the rate of vertical land motion, that is our model be-
 649 comes

$$\mathbf{m} = \begin{bmatrix} \mathbf{m}_{\text{sea}} \\ \mathbf{m}_{\text{land}} \end{bmatrix}, \quad (15)$$

650 where both \mathbf{m}_{sea} and \mathbf{m}_{land} are trans-dimensional models and for each we can choose
 651 to use either a Voronoi or Delaunay parameterization independently. Given observations
 652 of absolute sea level change, vertical land motion and tide gauges, the likelihood can be
 653 composed

$$p(\mathbf{d}|\mathbf{m}, \mathcal{I}) = p(\mathbf{d}_{\text{sea}}|\mathbf{m}_{\text{sea}}, \mathcal{I})p(\mathbf{d}_{\text{land}}|\mathbf{m}_{\text{land}}, \mathcal{I})p(\mathbf{d}_{\text{tide}}|\mathbf{m}_{\text{sea}}, \mathbf{m}_{\text{land}}, \mathcal{I}). \quad (16)$$

654 Note that the relative sea level surface is not directly parameterized and is derived
 655 from the two parameterized 2D fields. This still allows posterior inference on relative sea

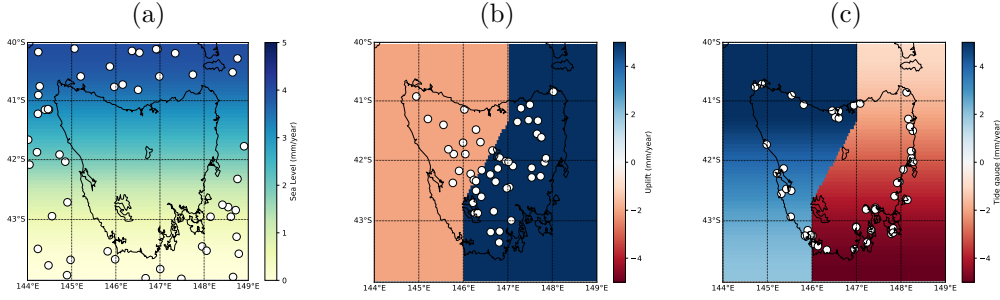
656 level rise as we can compute its 2D field for each model pair in the ensemble and collect
657 statistics as if it were parameterized independently.

658 For the choice of parameterization for the sea model, at long scale lengths, the rate
659 of sea level change at annual time scales is spatially smooth and predominantly corre-
660 lated with latitude. This strongly suggests that either of the two Delaunay parameter-
661 izations should be used to represent absolute sea level rise.

662 In contrast, the choice of parameterization for the land model is less evident. The
663 uplift of land is a combination of generally smooth variation cause by deformational pro-
664 cesses, but with strong lateral variations or discontinuities near active faults. If we as-
665 sume that the gradual variation is small compared to the magnitude of the discontinu-
666 ities near faults, then a Voronoi parameterization would be appropriate in tectonically
667 active regions. Either of the two Delaunay parameterizations would be more suited in
668 tectonically quiet regions.

669 In order to test the effect of different parameterization options, we set out to cre-
670 ate a synthetic data set for sea level and vertical land motion rates using the region of
671 Tasmania. In the following, “sea model” indicates absolute sea level rate (as observed
672 by satellite altimetry), “land model” indicates vertical land motion (as measured by GNSS
673 stations) and “tide gauge” indicates relative sea level rate (as measured by tide gauge
674 stations). For the sea model, the rate of absolute sea level rise is set to a smooth func-
675 tion of latitude between 0 and 4 mm/year. In order to sub sample the continuous field
676 into an irregular set of observations, sea level rate observations were created by gener-
677 ating random points in the ocean more than 10 km away from the coast line, sampling
678 the true (yet synthetic) sea level rate and adding independent Gaussian noise with a stan-
679 dard deviation of 1 mm/year.

680 For the synthetic land model, we created a fictitious fault running diagonally down
681 the center of Tasmania with a small negative uplift rate (-2.0 mm/year) on the western
682 side and a larger positive uplift rate (5.0 mm/year) to the east. Observations are gen-
683 erated using random points on land to which we add independent Gaussian noise with
684 a standard deviation of 1 mm/year. Lastly, we simply subtract the true sea model from
685 the true land model to obtain the tide gauge model and create observations randomly
686 located on the coast of Tasmania and add the same level of Gaussian noise. The syn-



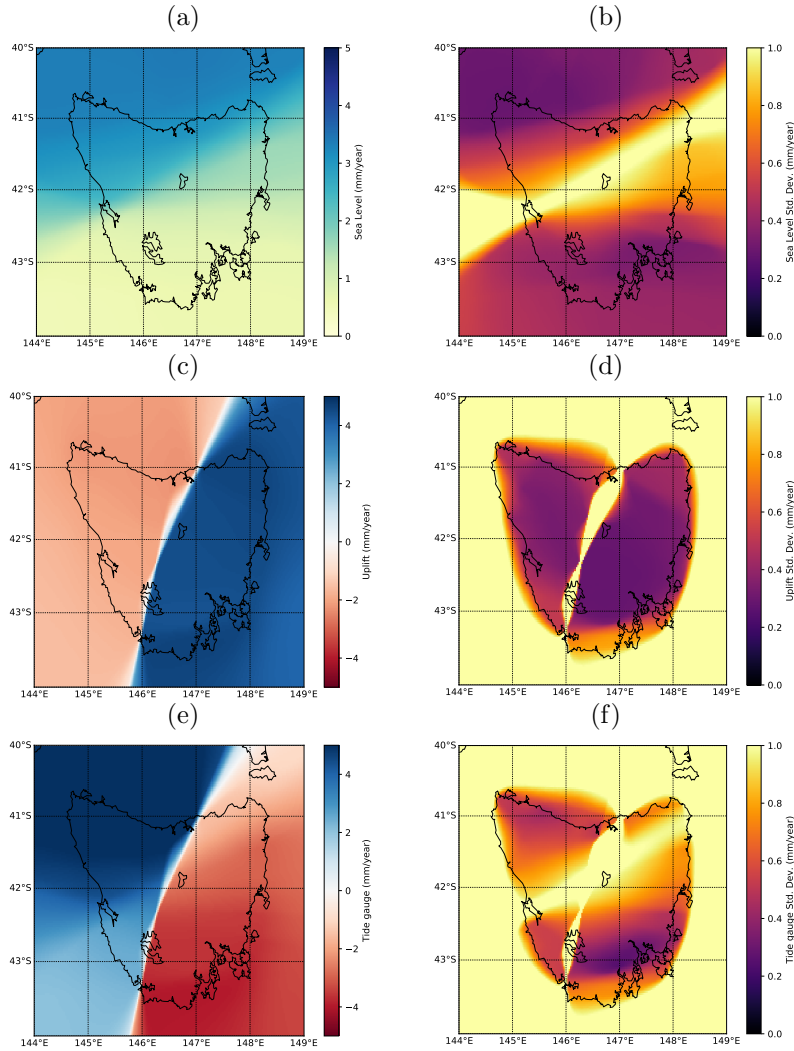
689 **Figure 9.** In (a) and (b) we show the true synthetic sea level rise and vertical land motion
 690 in mm/year. The derived tide gauge image is shown in (c). On each of the plots are shown the
 691 location of the randomly generated observations with small circles, that is the location of sea
 692 level observations are shown in (a), GPS observations in (b) and tide gauges in (c).

687 synthetic models are shown in Figure 9 in addition to the observations indicated with small
 688 circles of which there are 50 of each type for a total of 150 in this data set.

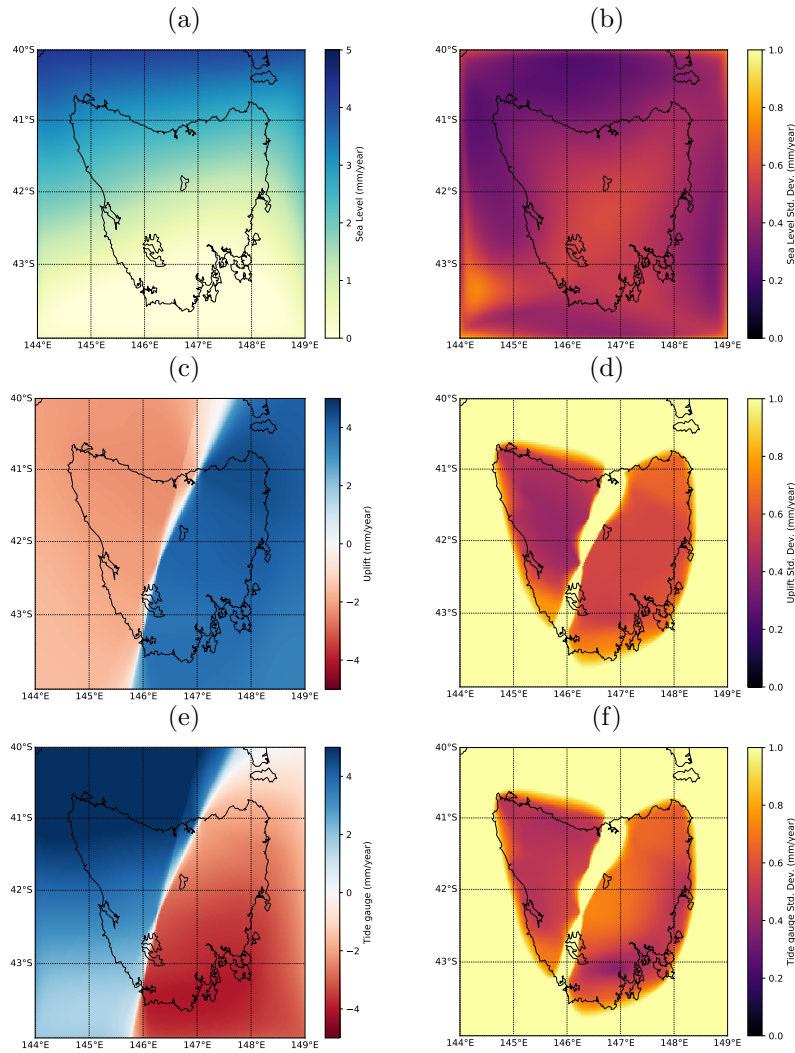
693 For this inversion, similar to the previous example, we use 28 Markov chains and
 694 4 temperatures logarithmically spaced between 1 and 5. Initial models are randomly gener-
 695 ated and chains are simulated for 1 million iterations with 500,000 removed as burn
 696 in. A primary difference here is that we use three independent hierarchical error scal-
 697 ing terms, one for each class of observation, namely sea level altimetry, land based GPS,
 698 and tide gauge.

699 For a first test, we invert the observations using a Voronoi cell parameterization
 700 for both the sea and land models with the results shown in Figure 10. As is to be ex-
 701 pected, the choice of the Voronoi cell parameterization for the sea level rate is a poor
 702 one that introduces large uncertainty in the sea level reconstruction in (b), which is then
 703 propagated to the derived tide gauge uncertainty in (f). For the recovery of the land model,
 704 the Voronoi cell parameterization is effective with high regions of uncertainty in the map
 705 restricted to the sea where there is no data, and along the fault where uncertainty in the
 706 faults location leads to multi-modality and therefore high standard deviation.

713 If we instead parameterize the sea with the Delaunay triangulation with linear in-
 714 terpolation, the results improve as shown in Figure 11. In (b) the standard deviation map
 715 of the sea level is lower, more homogeneous, and free of large magnitude standard de-
 716 viations caused by mobile Voronoi cells. This lower uncertainty propagates to the tide



707 **Figure 10.** In (a), (c) and (e) we show the ensemble means of the rates of absolute sea level
 708 change (sea), vertical land motion (land) and relative sea level change (tide gauge) in mm/year,
 709 when using a Voronoi cell parameterization for both the sea and land model. The corresponding
 710 standard deviation maps are shown in (b), (d), and (f). Large uncertainties in the tide gauge
 711 standard deviation are caused by using the Voronoi cell parameterization to represent the sea
 712 level.



719 **Figure 11.** In (a), (c) and (e) we show the ensemble means of the rates of absolute sea level
 720 change (sea), vertical land motion (land) and relative sea level change (tide gauge) in mm/year,
 721 when using the Delaunay parameterization with linear interpolation for the sea model and
 722 Voronoi parameterization for the land. The maps of standard deviation are shown in (b), (d),
 723 and (f).

717 gauge uncertainty shown in (f) where the remaining regions of high uncertainty are due
 718 to high uncertainty from the land model in the sea and along the fault.

724 To explore the posterior of the relative sea level, we can generate a series of vir-
 725 tual tide gauges evenly spaced along the coast line and show the posterior along the coast
 726 as done by Choblet et al. (2014). Note again that this is not a 2D field parameterized
 727 in this inversion but one that can be inferred directly from the parameterized 2D abso-
 728 lute sea level and vertical land motion surfaces. In Figure 12(a), we show a generated

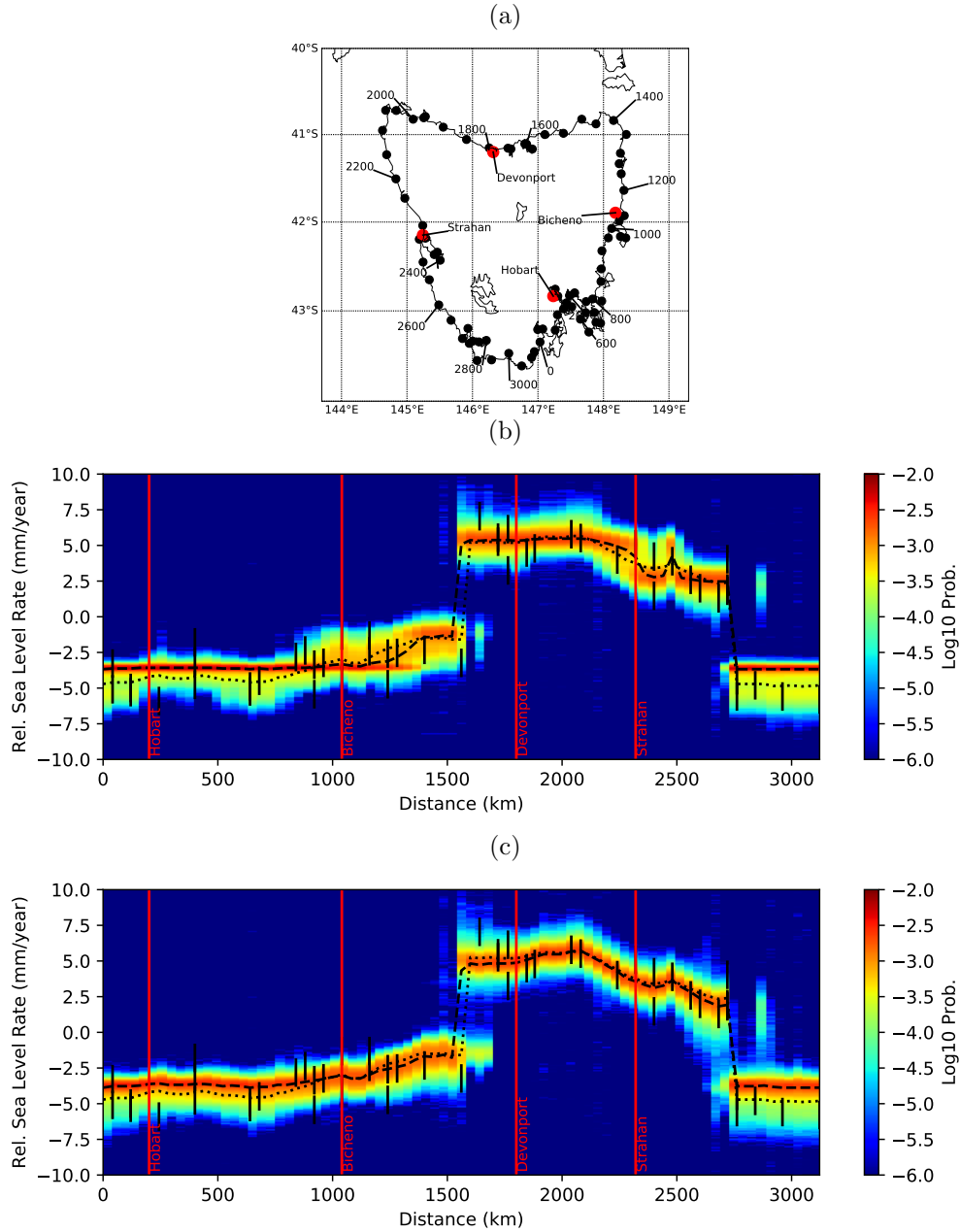
729 a set of points running counter clockwise around the coastline of Tasmania starting just
730 south of Hobart (the point marked as 0).

731 In Figure 12(b), the posterior histogram is shown for the inversion where the Voronoi
732 parameterization was used for both the sea and land model. Compared to the previous
733 example in Section 3, this posterior displays less multi-modality. Between Hobart and
734 Bicheno we can see a strong constant signal in the tide gauge due to the Voronoi param-
735 eterization fitting the gradual change in sea level along the East coast with a constant
736 function. In this case, the true model shown with a black dotted line is outside the re-
737 gions of highest posterior probability, although still within the more broader region of
738 probable models and therefore within uncertainties.

739 In Figure 12(c), the corresponding results for the inversion using the Delaunay tri-
740 angulation parameterization with linear interpolant are shown. In contrast to the pre-
741 vious results, the median and uncertainties more faithfully track the true model. This
742 is primarily due to the Delaunay parameterization being able to better model the grad-
743 ual variation in sea level rates along the East and West coasts. Inversions were also per-
744 formed with the Clough-Tocher interpolant with indistinguishable results relative to the
745 linear interpolant for this problem and these are not shown for brevity. This is due to
746 the relatively simple structure of the sea level which is equally well represented by lin-
747 ear and cubic interpolants given the level of noise.

756 5 Discussion

757 We have presented a new inversion software to constrain 2D fields using Bayesian
758 trans-dimensional sampling, and incorporating hierarchical error estimation, Hamilto-
759 nian Monte Carlo and Parallel Tempering. A novel aspect of this software is the choice
760 of alternate parameterizations rather than the commonly used Voronoi cell parameter-
761 ization. These alternate parameterizations are Delaunay triangulation with linear inter-
762 polation, and Delaunay triangulation with Clough-Tocher interpolation. In contrast to
763 Voronoi cells, which produce a discontinuous 2D field, these alternative parameteriza-
764 tions produce C^0 and C^1 continuous 2D fields respectively, and will allow applications
765 to problems where spatial gradients are required in either forward modelling or poste-
766 rior inferences.



748 **Figure 12.** In (a) we show the set of evenly spaced virtual tide gauge points starting at point
 749 0 south of Hobart and traversing the island in a counter clockwise sense. Selected points are
 750 marked with their approximate coastal distance in kilometers. In (b) we show the posterior dis-
 751 tribution of the virtual tide gauges for the inversion with the Voronoi cell parameterization for
 752 the sea model and in (c) with the Delaunay triangulation parameterization with linear inter-
 753 polant for the sea model. Both results use the Voronoi cell parameterization for the land model.
 754 In (b) and (c), the black dotted line is the true model, and the black dashed line is the median of
 755 the ensemble.

767 We showed in synthetic regression tests that the choice of parameterization is im-
768 portant as it both strongly affects the form of the posterior solution and the ability to
769 recover true models. We also stress that even in cases where the parameterization choice
770 is poor, the combination of trans-dimensional sampling and hierarchical error scaling en-
771 sures that while the posterior may contain poorer fitting models, the uncertainty esti-
772 mates will be higher and correctly estimated. For the Voronoi cell parameterization, we
773 showed that maps of standard deviation depict ring like structures with large magnitudes
774 that are caused by multi-modal posteriors, and which can be difficult to interpret. Some
775 have suggested these anomalies can be used as proxies for the location of discontinuities
776 (Burdick & Lekić, 2017; Cho et al., 2018; Olugboji et al., 2017), however they similarly
777 appear in synthetic tests of well converged posteriors when inverting known purely smooth
778 models, regardless of the number of chains (see Appendix B). Hence we urge caution this
779 interpretation of standard deviations: high standard deviations/multi-modalities in a Voronoi
780 cell based inversions is a necessary but not sufficient condition for the existence of a dis-
781 continuity.

782 In contrast, inversions using the two alternate Delaunay triangulation parameter-
783 izations exhibit far less propensity for multi-modal posteriors, even when these param-
784 eterizations are ill suited such as for the discontinuous 2D field regression example. This
785 leads to a more easily interpretable posterior. In some geophysical problems, the 1st or
786 2nd spatial derivative of the model may be important, in which case the Voronoi cell pa-
787 rameterization is inappropriate. The availability of this new software with these alter-
788 nate parameterizations will open up trans-dimensional sampling to a wider variety of geo-
789 physical inverse problems and also to fields beyond geosciences.

790 In a trans-dimensional inversion, it may seem surprising that the parameterization
791 can change the result of an inversion. For example, in the smooth model inversion, if the
792 model dimension can change, why does a Voronoi cell parameterization not simply con-
793 struct models with a large number of cells to approximate a smooth model? The key here
794 is that there is not enough information in the observations to constrain the required num-
795 ber of Voronoi cells to accurately reflect the smooth model. This contributes to the theo-
796 retical errors of the formulation as a “parameterization error” which is to some degree
797 approximated for in the hierarchical error estimation. If the inversions were simulated
798 by fixing the noise to the true value, the results would provide better fits to the mod-
799 els than shown. However, this type of inversion assumes perfect knowledge of the obser-

800 vational and theory errors which is generally not the case in geophysical inverse prob-
 801 lems.

802 In many geophysical problems, continuous models may be more appropriate than
 803 Voronoi cells. The poor representation of continuous fields of the Voronoi cell param-
 804 eterization was a primary motivation for the development of Trans-dimensional trees (Hawkins
 805 & Sambridge, 2015). Similar to this software, the trans-dimensional tree approach with
 806 a wavelet parameterization requires a choice of which wavelet basis to choose and results
 807 in similar large uncertainties when poor choices are made. At this stage, running sep-
 808 arate inversions and using approximate model choice criteria such as the DIC (Spiegel-
 809 halter, Best, Carlin, & van der Linde, 2002) to select which parameterization is better
 810 supported by the data seems a pragmatic albeit imperfect solution. Approximate cri-
 811 teria are not without their limitations and ultimately this could be resolved by accurate
 812 calculation of the evidence to compute Bayes factors, or by introducing some trans-dimensional
 813 method to propose local model parameterization changes.

814 **A Proposal Details**

815 **A.1 Move proposals**

816 Move proposals are standard MCMC proposals using a Metropolis-Hastings (Hast-
 817 ings, 1970; Metropolis et al., 1953) rule. The proposal moves one node/vertex at a time
 818 and uses a Gaussian perturbation of the point so that the proposal density is

$$Q(\mathbf{m} \rightarrow \mathbf{m}') = \frac{1}{k} N(0, \sigma_x) N(0, \sigma_y) \quad (\text{A.1})$$

819 where k is the number of nodes/vertices, and σ_x, σ_y are the standard deviations
 820 of the perturbations of the x and y coordinates of the node. Since the normal distribu-
 821 tion is symmetric, the proposal ratio in the acceptance criteria will cancel leaving the
 822 prior ratio and likelihood ratio. Furthermore, we use a uniform prior for the positions
 823 of the nodes and therefore this also cancels leaving the acceptance criteria for move pro-
 824 posals as simply the likelihood ratio, that is

$$\alpha_{\text{move}}(\mathbf{m} \rightarrow \mathbf{m}') = \min \left\{ 1, \frac{p(\mathbf{d}|\mathbf{m}', \mathcal{I})}{p(\mathbf{d}|\mathbf{m}, \mathcal{I})} \right\}. \quad (\text{A.2})$$

825 **A.2 Hamiltonian Steps**

826 Hamiltonian Monte Carlo proposals uses an auxiliary variable technique and cal-
 827 culation of the gradient of the posterior to generate new model proposals far away from
 828 the current model (Duane et al., 1987; Fichtner & Simut e, 2018; Neal, 2011; Sen & Biswas,
 829 2017).

830 The auxiliary variable, \mathbf{p} , is analogous to momentum in a Hamiltonian dynamical
 831 system

$$\mathcal{H}(\mathbf{m}, \mathbf{p}) = U(\mathbf{m}) + K(\mathbf{p}), \quad (\text{A.3})$$

832 where U is the potential function of the current model \mathbf{m} , and K the kinetic en-
 833 ergy function of the momentum \mathbf{p} . The potential function is given by

$$U(\mathbf{m}) = -\log p(\mathbf{d}|\mathbf{m}, \mathcal{I})p(\mathbf{m}|\mathcal{I}), \quad (\text{A.4})$$

834 that is, the negative log of the posterior and the kinetic energy function by

$$K(\mathbf{p}) = \frac{\mathbf{p}^T \mathbf{M} \mathbf{p}}{2}, \quad (\text{A.5})$$

835 where \mathbf{M} is the mass matrix. Recent advances in HMC (Fichtner et al., 2019) have
 836 shown that this mass matrix can be optimized to provide better sampling in fixed di-
 837 mension inversions. In trans-dimensional sampling, the number of model parameters and
 838 hence the size of this mass matrix changes during the inversion so we have elected to use
 839 an identity matrix here. The approach implemented here could be improved further by
 840 further research into adapting optimal mass matrices trans-dimensional sampling.

841 A Hamiltonian Monte Carlo proposal samples an initial momentum vector \mathbf{p} from
 842 a multi-dimensional normal distribution with zero mean and unit standard deviation.
 843 The Hamiltonian dynamical system is simulated for a configured number of steps with
 844 a tunable step size to obtain a proposed model \mathbf{m}' and momentum \mathbf{p}' . This simulation
 845 requires the gradient of the potential function, $\frac{\partial U}{\partial \mathbf{m}}$, and to ensure that the proposal is
 846 reversible, the leap frog method is generally used (Neal, 2011).

847 In the cases of the three parameterizations used, Hamiltonian proposals only per-
 848 turb the values at each of the Voronoi cell nodes/Delaunay triangulation vertices and
 849 not their locations. This is due to the fact that the gradient of the likelihood with re-
 850 spect to the location of the cells is undefined for Voronoi cells.

851 Once a proposed model is obtained, it is accepted or rejected according to the cri-
 852 teria

$$\alpha_{\text{hmc}}(\mathbf{m} \rightarrow \mathbf{m}') = \min \{1, \exp(-\mathcal{H}(\mathbf{m}, \mathbf{p}) + \mathcal{H}(\mathbf{m}', \mathbf{p}'))\}. \quad (\text{A.6})$$

853 The requirement of needing the gradient of the posterior with respect to the model
 854 parameter values may be prohibitive to compute or not available in some cases. The soft-
 855 ware frame also supports standard McMC proposal for change of values and the accep-
 856 tance criteria for value proposals in this case is similar to the move proposal above.

857 **A.3 Trans-dimensional Steps**

858 In this software, trans-dimensional steps involve adding and remove nodes and their
 859 values. For simplicity, we have chosen to use the “birth from the prior” approach. In this
 860 approach, for a Birth proposal where a new node is generated, the new location and value
 861 are sampled from the prior. This means that the proposal density for a Birth proposal
 862 is

$$Q(\mathbf{m} \rightarrow \mathbf{m}') = p(x')p(y')p(z') \quad (\text{A.7})$$

863 where x' and y' are the new node coordinates and z' the new node value. This strat-
 864 egy simplifies the Birth and Death acceptance criteria in two ways: first the proposal ra-
 865 tio cancels with the prior ratio and secondly the Jacobian is unity. This leaves an ac-
 866 ceptance criteria for birth/death proposals as simply the likelihood ratio, that is

$$\alpha_{\text{birth/death}} = \min \left\{ 1, \frac{p(\mathbf{d}|\mathbf{m}', \mathcal{I})}{p(\mathbf{d}|\mathbf{m}, \mathcal{I})} \right\}. \quad (\text{A.8})$$

867 **A.4 Hierarchical proposals**

868 For hierarchical error scaling proposals, we use a standard MCMC proposal with
 869 a normal distribution perturbation of λ and the acceptance criteria therefore is

$$\alpha_\lambda(\lambda \rightarrow \lambda') = \min \left\{ 1, \frac{p(\lambda') p(\mathbf{d}|\mathbf{m}', \mathcal{I})}{p(\lambda) p(\mathbf{d}|\mathbf{m}, \mathcal{I})} \right\}, \quad (\text{A.9})$$

870 where $p(\lambda)$ is the prior on the hierarchical scaling factor.

871 **A.5 Parallel tempering**

872 During a Parallel Tempering exchange proposal, two parallel chains are chosen at
 873 random to exchange their models. The acceptance criteria is

$$\alpha_{\text{exchange}}(\mathbf{m}_i \leftrightarrow \mathbf{m}_j) = \min \left\{ 1, \frac{[p(\mathbf{d}|\mathbf{m}_j, \mathcal{I})]^{\frac{1}{T_i}}}{[p(\mathbf{d}|\mathbf{m}_i, \mathcal{I})]^{\frac{1}{T_i}}} \frac{[p(\mathbf{d}|\mathbf{m}_i, \mathcal{I})]^{\frac{1}{T_j}}}{[p(\mathbf{d}|\mathbf{m}_j, \mathcal{I})]^{\frac{1}{T_j}}} \right\} \quad (\text{A.10})$$

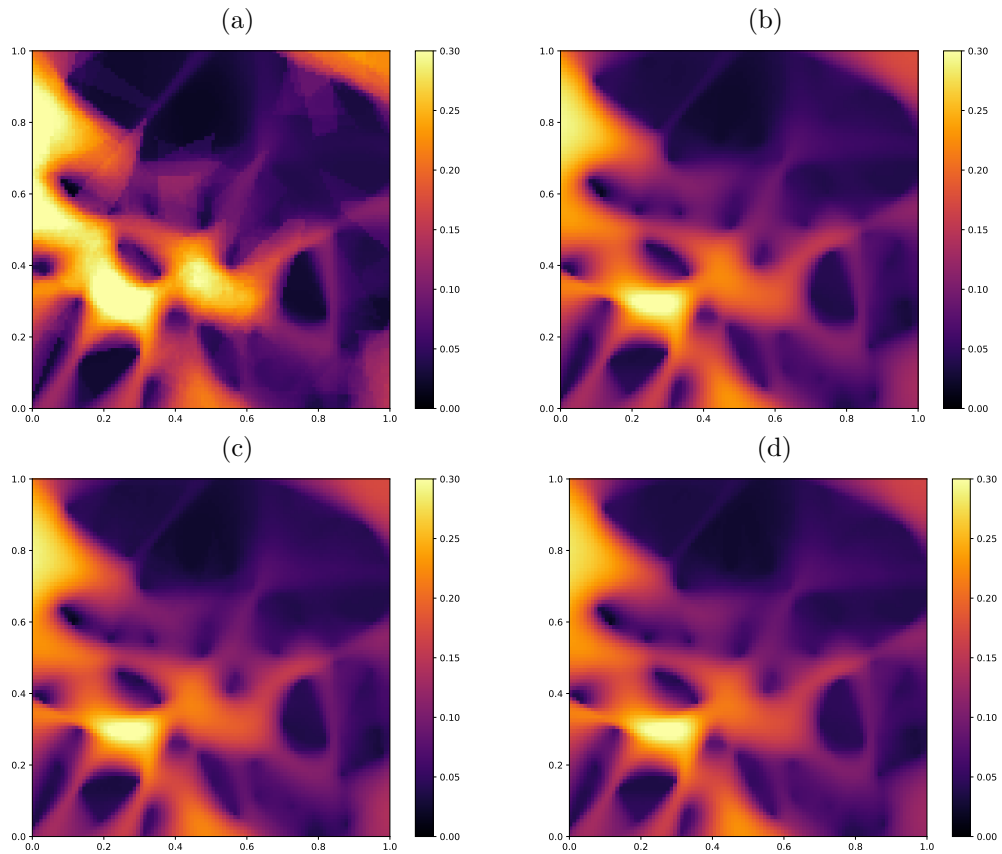
874 where i and j subscripts indicate the two different chains.

875 **B Stability of variance estimates**

876 In this short appendix we show the variance estimate for the regression problem
 877 of the smooth model with Voronoi cell parameterization under different configurations
 878 of the inversion. In Figure B.1(a) we show the result from a single chain, (b) the same
 879 number of chains as the main result (28) but we use 10 million iterations instead of 1
 880 million, (c) 56 chains and (d) 112 chains. In each case, the same pattern of variance as
 881 presented in Figure 3(b) is recovered indicating that our presented results are well con-
 882 verged and provide robust estimate of the posterior variance. Hence the posterior multi-
 883 modalities as discussed are robust features and not due to poor convergence.

888 **Acknowledgments**

889 Portions of this software development were funded by AuScope through the Na-
 890 tional Collaborative Research Infrastructure Strategy (NCRIS), an Australian Federal
 891 Government programme.



884 **Figure B.1.** A comparison of the the standard deviation obtained from differently config-
885 ure inversions. In (a) we invert a single chain, (b) we use 28 independent chains as in the main
886 body but simulate 10 million steps, in (c) we use 56 chains and (d) 112 chains. In each case the
887 estimated standard deviation is in agreement with results presented in Figure 3(b)

892 RH and TB are funded by the European Unions Horizon 2020 research and inno-
 893 vation programme under Grant Agreement No. 716542.

894 The authors kindly thank Nicklas Linde, Andreas Fichtner and an anonymous re-
 895 viewer for the constructive comments that helped to improve this manuscript.

896 The TransTessellate2D software is available from <http://www.earth.org.au>

897 References

- 898 Akaike, H. (1974). A new look at the statistical model identification. *IEEE Transac-*
 899 *tions on Automatic Control, AC-19*(6), 716-723.
- 900 Al-Awadhi, F., Hurn, M., & Jennison, C. (2004). Improving the acceptance rate of
 901 reversible jump MCMC proposals. *Statistics and Probability Letters, 69*, 189 -
 902 198.
- 903 Backus, G. (1970a). Inference from inadequate and inaccurate data I. *Proceedings of*
 904 *the National Academy of Sciences, 65*(1), 1-7.
- 905 Backus, G. (1970b). Inference from inadequate and inaccurate data II. *Proceedings*
 906 *of the National Academy of Sciences, 65*(2), 281-287.
- 907 Backus, G. (1970c). Inference from inadequate and inaccurate data III. *Proceedings*
 908 *of the National Academy of Sciences, 67*(1), 282-289.
- 909 Bayes, T. (1763). An essay towards solving a problem in the doctrine of chances.
 910 *Philosophical Transactions of the Royal Society, 53*, 370-418.
- 911 Belhadj, J., Romary, T., Gesret, A., Noble, M., & Figliuzzu, B. (2018). New param-
 912 eterizations for bayesian seismic tomography. *Inverse Problems, 34*(6).
- 913 Billings, S., Beatson, R., & Newsam, G. (2002). Interpolation of geophysical data us-
 914 ing continuous global surfaces. *Geophysics, 67*(6), 1810 - 1822.
- 915 Blewitt, G., Kreemer, C., Hammond, W. C., & Gazeaux, J. (2015). MIDAS ro-
 916 bust trend estimator for accurate gps station velocities without step detection.
 917 *Journal of Geophysical Research: Solid Earth, 121*(3), 2054-2068.
- 918 Bodin, T., Salmon, M., Kennett, B. L. N., & Sambridge, M. (2012). Proba-
 919 bilistic surface reconstruction from multiple data sets: An example for the
 920 Australian Moho. *Journal of Geophysical Research, 117*, B10307. doi:
 921 1029/2012JB009547
- 922 Bodin, T., & Sambridge, M. (2009). Seismic tomography with the reversible jump

- 923 algorithm. *Geophysical Journal International*, *178*, 1411 - 1436.
- 924 Bodin, T., Sambridge, M., Tkalčić, H., Arroucau, P., Gallagher, L., & Rawlin-
 925 son, N. (2012). Trans-dimensional inversion of receiver functions and sur-
 926 face wave dispersion. *Journal of Geophysical Research*, *117*, B02301. doi:
 927 10.1029/2011JB008560
- 928 Brooks, S., Gelman, A., Jones, G. L., & Meng, X. (Eds.). (2011). *Handbook of*
 929 *markov chain monte carlo*. Chapman and Hall/CRC.
- 930 Brunetti, C., Linde, N., & Vrugt, J. A. (2017). Bayesian model selection in hydro-
 931 geophysics: Application to conceptual subsurface models of the South Oyster
 932 Bacterial Transport Site, Virginia, USA. *Advances in Water Resources*, *102*,
 933 127 - 141.
- 934 Burdick, S., & Lekić, V. (2017). Velocity variations and uncertainty from transdi-
 935 mensional P-wave tomography of North America. *Geophysical Journal Interna-*
 936 *tional*, *209*(2), 1337 - 1351.
- 937 Cazenave, A., & Cozannet, G. L. (2013). Sea level rise and its coastal impacts.
 938 *Earth's Future*, *2*, 15 - 34.
- 939 Chiao, L., & Kuo, B. (2001). Multiscale seismic tomography. *Geophysical Journal*
 940 *International*, *145*, 517 - 527.
- 941 Cho, Y., Gibson, R. L., & Zhu, D. (2018). Quasi 3D transdimensional Markov-chain
 942 Monte Carlo for seismic impedance inversion and uncertainty analysis. *Inter-*
 943 *pretation*, *6*(3), T613 - T624. doi: 10.1190/INT-2017-0136.1
- 944 Choblet, G., Husson, L., & Bodin, T. (2014). Probabilistic surface reconstruction of
 945 coastal sea level rise during the twentieth century. *Journal of Geophysical Re-*
 946 *search: Solid Earth*, *119*(12), 9206 - 9236. doi: 10.1002/2014JB011639
- 947 Church, J. A., & White, N. J. (2011). Sea-level rise from the late 19th to the early
 948 21st century. *Surv. Geophys.*, *32*, 585 - 602.
- 949 Clough, R. W., & Tocher, J. L. (1965). Finite element stiffness matrices for anal-
 950 ysis of plate bending. *Proceedings of Conference on Matrix Methods in Struc-*
 951 *tural Analysis*.
- 952 Davies, J. H. (2013). Global map of solid Earth surface heat flow. *Geochemistry*
 953 *Geophysics Geosystems*, *14*(10), 4608 - 4622. doi: 10.1002/ggge.20271
- 954 Denison, D. G. T., Holmes, C. C., Mallick, B. K., & Smith, A. F. M. (2002).
 955 *Bayesian methods for non-linear classification and regression*. John Wiley

- 956 and Sons.
- 957 de Pasquale, G., & Linde, N. (2017). On structure-based priors in Bayesian geophys-
- 958 ical inversion. *Geophysical Journal International*, *208*(3), 1342 - 1358.
- 959 Dettmer, J., Benavente, R., Cummins, P. R., & Sambridge, M. (2014). Trans-
- 960 dimensional finite-fault inversion. *Geophysical Journal International*, *199*,
- 961 735-751.
- 962 Dettmer, J., Dosso, S. E., & Holland, C. W. (2011). Sequential trans-dimensional
- 963 Monte Carlo for range-dependent geoacoustic inversion. *J. Acoust. Soc. Am.*,
- 964 *129*(4), 1794-1806.
- 965 Dettmer, J., Hawkins, R., Cummins, P. R., Hossen, J., Sambridge, M., Hino, R., &
- 966 Inazu, D. (2016). Tsunami source uncertainty estimation: The 2011 Japan
- 967 tsunami. *Journal of Geophysical Research: Solid Earth*, *121*, 4483 - 4505. doi:
- 968 10.1002/2015JB012764
- 969 Dettmer, J., Molnar, S., Steininger, G., Dosso, S. E., & Cassidy, J. F. (2012). Trans-
- 970 dimensional inversion of microtremor array dispersion data with hierarchical
- 971 autoregressive error models. *Geophysical Journal International*, *188*, 719 -
- 972 734.
- 973 Dosso, S. E., Holland, C. W., & Sambridge, M. (2012). Parallel tempering in
- 974 strongly nonlinear geoacoustic inversion. *Journal of the Acoustic Society of*
- 975 *America*, *132*(5), 3030-3040.
- 976 Dosso, S. E., & Wilmut, M. J. (2006). Data uncertainty estimation in matched-field
- 977 geoacoustic inversion. *IEEE Journal of Oceanic Engineering*, *31*(2), 470 - 479.
- 978 Duane, S., Kennedy, A. D., Pendelton, B. J., & Roweth, D. (1987). Hybrid Monte
- 979 Carlo. *Physics Letters B*, *195*(2), 216 - 222.
- 980 Earl, D. J., & Deem, M. W. (2005). Parallel tempering: Theory, applications, and
- 981 new perspectives. *Physical Chemistry Chemical Physics*, *7*(23), 3910-3916.
- 982 Fichtner, A., & Simutè, S. (2018). Hamiltonian monte carlo inversion of seismic
- 983 sources in complex media. *Journal of Geophysical Research: Solid Earth*,
- 984 *123*(4), 2984 - 2999. doi: 10.1002/2017JB015249
- 985 Fichtner, A., Zunini, A., & Gebraad, L. (2019). Hamiltonian Monte Carlo solution of
- 986 tomographic inverse problems. *Geophysical Journal International*, *216*(2), 1344
- 987 - 1363. doi: 10.1093/gji/ggy496
- 988 Galetti, E., Curtis, A., Baptie, B., Jenkins, D., & Nicolson, H. (2016). Transdimen-

- 989 sional Love-wave tomography of the British Isles and shear-velocity structure
 990 of the East Irish Sea Basin from ambient-noise interferometry. *Geophysical*
 991 *Journal International*. doi: 10.1093/gji/ggw286
- 992 Galetti, E., Curtis, A., Meles, G. A., & Baptie, B. (2015). Uncertainty loops in
 993 travel-time tomography from nonlinear wave physics. *Physical Review Letters*,
 994 *114*, 148501. doi: 10.1103/PhysRevLett.114.148501
- 995 Gao, C., & Lekić, V. (2018). Consequences of parametrization choices in surface
 996 wave inversion: insights from transdimensional Bayesian methods. *Geophysical*
 997 *Journal International*, *215*(2), 1037 - 1063.
- 998 Gelman, A., & Rubin, D. B. (1992). Inference from iterative simulation using multi-
 999 ple sequences. *Statistical Science*, *7*(4), 457 - 472.
- 1000 Geyer, C. J., & Møller, J. (1994). Simulation procedures and likelihood inference for
 1001 spatial point processes. *Scandinavian Journal of Statistics*, *21*, 359-373.
- 1002 Gommenginger, C., Thibaut, P., Fenoglio-Marc, L., Quartly, G., Deng, X., Gómez-
 1003 Enri, J., . . . Gao, Y. (2011). Coastal altimetry. In S. Vignudelli, A. Kos-
 1004 tianoy, & P. Cipollini (Eds.), (chap. Retracking Altimeter Waveforms Near the
 1005 Coasts). Springer.
- 1006 Green, P. J. (1995). Reversible jump Markov chain Monte Carlo computation and
 1007 Bayesian model determination. *Biometrika*, *82*(4), 711 - 732.
- 1008 Hanke, M. (1996). Limitations of the L-curve method in ill-posed problems. *BIT*
 1009 *Numerical Mathematics*, *36*(2), 287-301.
- 1010 Hansen, P. C. (1999). *The l-curve and its use in the numerical treatment of in-*
 1011 *verse problems*. Department of Mathematical Modelling, Technical University
 1012 of Denmark.
- 1013 Hastings, W. K. (1970). Monte Carlo sampling methods using Markov chains and
 1014 their applications. *Biometrika*, *57*(1), 97 - 109.
- 1015 Hawkins, R., Brodie, R., & Sambridge, M. (2017). Bayesian trans-dimensional in-
 1016 version of Airborne Electromagnetic 2D conductivity profiles. *Exploration Geo-*
 1017 *physics*. doi: 10.1071/EG16139
- 1018 Hawkins, R., & Sambridge, M. (2015). Geophysical imaging using trans-dimensional
 1019 trees. *Geophysical Journal International*, *203*(2), 972-1000. doi: 10.1093/gji/
 1020 gg326
- 1021 Hopcroft, P. O., Gallagher, K., & Pain, C. C. (2007). Inference of past climate

- 1022 from borehole temperature data using Bayesian reversible jump Markov chain
 1023 Monte Carlo. *Geophysical Journal International*, 171(3), 1430-1439. doi:
 1024 10.1111/j.1365-246X.2007.03596.x
- 1025 Hopcroft, P. O., Gallagher, K., & Pain, C. C. (2009). A bayesian partition mod-
 1026 elling approach to resolve spatial variability in climate records from borehole
 1027 temperature inversion. *Geophysical Journal International*, 178(2), 651-666.
 1028 doi: 10.1111/j.1365-246X.2009.04192.x
- 1029 Husson, L., Bodin, T., Spada, G., Choblet, G., & Comé, K. (2018). Bayesian surface
 1030 reconstruction of geodetic uplift rates: mapping the global fingerprint of gia.
 1031 *Journal of Geodynamics*, 122, 25 - 40.
- 1032 Ingham, E. M., Heslop, D., Roberts, A. P., Hawkins, R., & Sambridge, M. (2014).
 1033 Is there a link between geomagnetic reversal frequency and paleointensity? a
 1034 bayesian approach. *Journal of Geophysical Research: Solid Earth*, 119(7), 5290
 1035 - 5304. doi: 10.1002/2014JB010947
- 1036 Inoue, H., Fukao, Y., Tanabe, K., & Ogata, Y. (1990). Whole mantle P-wave travel
 1037 time tomography. *Phys. Earth Planet. Inter.*, 59, 294 - 328.
- 1038 Káráson, H., & van der Hilst, R. D. (2001). Tomographic imaging of the lower-
 1039 most mantle with differential times of refracted and diffracted core phases
 1040 (PKP,P_{diff}). *Journal of Geophysical Research*, 106(B4), 6569-6587.
- 1041 Kass, R. E., & Raftery, A. E. (1995). Bayes factors. *Journal of the American Statis-
 1042 tical Association*, 90(430), 773-795.
- 1043 Kolb, J. M., & Lekić, V. (2014). Receiver function deconvolution using transdi-
 1044 mensional hierarchical Bayesian inference. *Geophysical Journal International*,
 1045 197(3), 1719 - 1735.
- 1046 Lochbühler, T., Vrugt, J. A., Sadegh, M., & Linde, N. (2015). Summary statistics
 1047 from training images as prior information in probabilistic inversion. *Geophysi-
 1048 cal Journal International*, 201(1), 157-171.
- 1049 Malinverno, A. (2002). Parsimonious Bayesian Markov chain Monte Carlo inversion
 1050 in a nonlinear geophysical problem. *Geophysical Journal International*, 151,
 1051 675-688.
- 1052 Malinverno, A., & Briggs, V. A. (2004). Expanded uncertainty quantification in
 1053 inverse problems: Hierarchical Bayes and empirical Bayes. *Geophysics*, 69(4),
 1054 1005 - 1016. doi: 10.1190/1.1778243

- 1055 Mann, S. (1998). *Cubic precision Clough-Tocher interpolation* (Tech. Rep. No. CS-
1056 98-15). Computer Science Department, University of Waterloo.
- 1057 Metropolis, N., Rosenbluth, A. W., Rosenbluth, M. N., Teller, A. H., & Teller, E.
1058 (1953). Equation of state calculations by fast computing machines. *The*
1059 *Journal of Chemical Physics*, *21*(6), 1986-1992.
- 1060 Mosegaard, K., & Tarantola, A. (1995). Monte Carlo sampling of solutions to inverse
1061 problems. *Journal of Geophysical Research*, *100*(B7), 12431-12447.
- 1062 Neal, R. M. (1994). An improved acceptance procedure for the hybrid Monte Carlo
1063 algorithm. *Journal of Computational Physics*, *111*, 194 - 203.
- 1064 Neal, R. M. (2011). Handbook of Markov chain Monte Carlo. In (chap. MCMC using
1065 Hamiltonian Dynamics). Chapman and Hall/CRC.
- 1066 Oliver, M. A., & Webster, R. (1990). Kriging: a method of interpolation for geo-
1067 graphical information systems. *International Journal of Geographical Informa-*
1068 *tion Systems*, *4*(3), 313-332.
- 1069 Olugboji, T. M., Lekic, V., & McDonough, W. (2017). A statistical assessment
1070 of seismic models of the U.S. continental crust using Bayesian inversion of
1071 ambient noise surface wave dispersion data. *Tectonics*, *36*.
- 1072 Pfeffer, J., & Allemand, P. (2016). The key role of vertical land motions in coastal
1073 sea level variations: A global synthesis of multisatellite altimetry, tide gauge
1074 data and GPS measurements. *Earth and Planetary Science Letters*, *439*, 39 -
1075 47.
- 1076 Pfeffer, J., Spada, G., Mémin, A., Boy, J.-P., & Allemand, P. (2017). Decoding the
1077 origins of vertical land motions observed today at coasts. *Geophysical Journal*
1078 *International*, *210*, 148 - 165.
- 1079 Piana Agostinetti, N., Giacomuzzi, G., & Malinverno, A. (2015). Local 3D earth-
1080 quake tomography by trans-dimensional Monte Carlo sampling. *Geophysical*
1081 *Journal International*, *201*(3), 1598-1617.
- 1082 Piana Agostinetti, N., & Malinverno, A. (2010). Receiver function inversion by
1083 trans-dimensional Monte Carlo sampling. *Geophysical Journal International*,
1084 *181*(2), 858-872.
- 1085 Pijpers, F. P., & Thompson, M. J. (1992). Faster formulations of the optimally
1086 localized averages method for helioseismic inversions. *Astronomy and Astro-*
1087 *physics*, *262*, L33 - L36.

- 1088 Rawlinson, N., Fichtner, A., Sambridge, M., & Young, M. (2014). Advances in geo-
 1089 physics. In (Vol. 55, chap. Seismic tomography and the assessment of uncer-
 1090 tainty). Academic Press.
- 1091 Ray, A., & Key, K. (2012). Bayesian inversion of marine CSEM data with a trans-
 1092 dimensional self parametrizing algorithm. *Geophysical Journal International*,
 1093 *191*, 1135 - 1151. doi: 10.1111/j.1365-246X.2012.05677.x
- 1094 Roy, C., & Romanowicz, B. A. (2017). On the implications of a priori constraints in
 1095 transdimensional Bayesian inversion for continental lithospheric layering. *Jour-
 1096 nal of Geophysical Research: Solid Earth*, *122*, 10118 - 10131.
- 1097 Sambridge, M. (2014). A parallel tempering algorithm for probabilistic sampling and
 1098 multimodal optimization. *Geophysical Journal International*, *192*, 357-374.
- 1099 Sambridge, M., Braun, J., & McQueen, H. (1995). Geophysical parameterization
 1100 and interpolation of irregular data using natural neighbours. *Geophysical Jour-
 1101 nal International*, *122*, 837-857.
- 1102 Sambridge, M., & Faletić, R. (2003). Adaptive whole earth tomography. *Geochem-
 1103 istry Geophysics Geosystems*, *4*(3).
- 1104 Sambridge, M., Gallagher, K., Jackson, A., & Rickwood, P. (2006). Trans-
 1105 dimensional inverse problems, model comparison and the evidence. *Geophysical
 1106 Journal International*, *167*, 528-542.
- 1107 Sambridge, M., & Mosegaard, K. (2002). Monte Carlo methods in geophysical in-
 1108 verse problems. *Reviews of Geophysics*, *40*(3), 1-29.
- 1109 Sandwell, D. T., & Smith, W. H. F. (1997). Marine gravity anomaly from Geosat
 1110 and ERS 1 satellite altimetry. *J. Geophys. Res.*, *102*, 10,039 - 10,054.
- 1111 Saygin, E., Cummins, P., Cipta, A., Hawkins, R., Pandhu, R., Murjaya, J., . . . Ken-
 1112 nett, B. L. N. (2016). Imaging architecture of the Jakarta basin, Indonesia
 1113 with trans-dimensional Bayesian seismic noise tomography. *Geophysical Jour-
 1114 nal International*, *204*(2), 918 - 931. doi: 10.1093/gji/ggv466
- 1115 Schöniger, A., Wöhling, T., Samaniego, L., & Nowak, W. (2014). Model selection
 1116 on solid ground: Rigorous comparison of nine ways to evaluate Bayesian model
 1117 evidence. *Water Resour. Res.*, *50*, 9484 - 9513.
- 1118 Schwarz, G. E. (1978). Estimating the dimension of a model. *Annals of Statistics*,
 1119 *6*(2), 461-464.
- 1120 Sen, M. K., & Biswas, R. (2017). Transdimensional seismic inversion using the re-

- 1121 versible jump Hamiltonian Monte Carlo algorithm. *Geophysics*, 82(3), R119 -
1122 R134. doi: 10.1190/GEO2016-0010.1
- 1123 Spiegelhalter, D. J., Best, N. G., Carlin, B. P., & van der Linde, A. (2002). Bayesian
1124 measures of model complexity and fit. *Journal of the Royal Statistical Society:
1125 Series B*, 64, 583-639.
- 1126 Steininger, G., Dosso, S. E., Holland, C. W., & Dettmer, J. (2014). Estimating
1127 seabed scattering mechanisms via Bayesian model selection. *J. Acoust. Soc.
1128 Am.*, 136(4), 1552-1562.
- 1129 Valentine, A. P., & Sambridge, M. (2018). Optimal regularisation for a class of lin-
1130 ear inverse problem. *Geophysical Journal International*, ggy303. doi: 10.1093/
1131 gji/ggy303
- 1132 Zaroli, C. (2016). Global seismic tomography using Backus-Gilbert inversion. *Geo-
1133 physical Journal International*, 207, 876-888.